

## RESEARCH ARTICLE

10.1002/2016JD026078

## Key Points:

- Ozone structures associated with a cold front passage
- Simultaneous ozone lidar, ozonesonde, aerosol lidar, and airborne in situ measurements
- Mixed influence of biomass burning and stratosphere-to-troposphere transport on tropospheric ozone

## Correspondence to:

S. Kuang,  
kuang@nsstc.uah.edu

## Citation:

Kuang, S., et al. (2017), Summertime tropospheric ozone enhancement associated with a cold front passage due to stratosphere-to-troposphere transport and biomass burning: Simultaneous ground-based lidar and airborne measurements, *J. Geophys. Res. Atmos.*, 122, 1293–1311, doi:10.1002/2016JD026078.




Received 11 OCT 2016

Accepted 4 JAN 2017

Accepted article online 5 JAN 2017

Published online 24 JAN 2017

## Summertime tropospheric ozone enhancement associated with a cold front passage due to stratosphere-to-troposphere transport and biomass burning: Simultaneous ground-based lidar and airborne measurements

Shi Kuang<sup>1</sup> , Michael J. Newchurch<sup>2</sup> , Matthew S. Johnson<sup>3</sup> , Lihua Wang<sup>1</sup>, John Burris<sup>4,5</sup>, Robert B. Pierce<sup>6</sup> , Edwin W. Eloranta<sup>7</sup> , Ilana B. Pollack<sup>8,9,10</sup> , Martin Graus<sup>8,9,11</sup>, Joost de Gouw<sup>8,9</sup> , Carsten Warneke<sup>8,9</sup> , Thomas B. Ryerson<sup>8</sup> , Milos Z. Markovic<sup>8,12</sup>, John S. Holloway<sup>8,9</sup>, Arastoo Pour-Biazar<sup>1</sup>, Guanyu Huang<sup>2,13</sup> , Xiong Liu<sup>14</sup> , and Nan Feng<sup>2</sup> 

<sup>1</sup>Earth System Science Center, University of Alabama in Huntsville, Huntsville, Alabama, USA, <sup>2</sup>Atmospheric Science Department, University of Alabama in Huntsville, Huntsville, Alabama, USA, <sup>3</sup>Earth Science Division, NASA Ames Research Center, Moffett Field, California, USA, <sup>4</sup>NASA Goddard Space Flight Center, Greenbelt, Maryland, USA, <sup>5</sup>Currently retired, <sup>6</sup>NOAA NESDIS Center for Satellite Applications and Research, Madison, Wisconsin, USA, <sup>7</sup>Space Science and Engineering Center, University of Wisconsin-Madison, Madison, Wisconsin, USA, <sup>8</sup>Chemical Sciences Division, NOAA Earth System Research laboratory, Boulder, Colorado, USA, <sup>9</sup>Now at Department of Atmospheric Science, Colorado State University, Fort Collins, Colorado, USA, <sup>10</sup>Cooperative Institute for Research in Environmental Sciences, University of Colorado Boulder, Boulder, Colorado, USA, <sup>11</sup>Now at Institute of Atmospheric and Cryospheric Sciences, Innsbruck University, Innsbruck, Austria, <sup>12</sup>Now at Air Quality Research Division, Environment and Climate Change Canada, Toronto, Ontario, Canada, <sup>13</sup>Now at Atomic and Molecular Physics Division, Harvard Smithsonian Center for Astrophysics, Cambridge, Massachusetts, USA, <sup>14</sup>Atomic and Molecular Physics Division, Harvard Smithsonian Center for Astrophysics, Cambridge, Massachusetts, USA

**Abstract** Stratosphere-to-troposphere transport (STT) and biomass burning (BB) are two important natural sources for tropospheric ozone that can result in elevated ozone and air-quality episode events. High-resolution observations of multiple related species are critical for complex ozone source attribution. In this article, we present an analysis of coinciding ground-based and airborne observations, including ozone lidar, ozonesonde, high spectral resolution lidar (HSRL), and multiple airborne in situ measurements, made on 28 and 29 June 2013 during the Southeast Nexus field campaign. The ozone lidar and HSRL reveal detailed ozone and aerosol structures as well as the temporal evolution associated with a cold front passage. The observations also captured two enhanced (+30 ppbv) ozone layers in the free troposphere (FT), which were determined from this study to be caused by a mixture of BB and stratospheric sources. The mechanism for this STT is tropopause folding associated with a cutoff upper level low-pressure system according to the analysis of its potential vorticity structure. The depth of the tropopause fold appears to be shallow for this case compared to events observed in other seasons; however, the impact on lower tropospheric ozone was clearly observed. This event suggests that strong STT may occur in the southeast United States during the summer and can potentially impact lower troposphere during these times. Statistical analysis of the airborne observations of trace gases suggests a coincident influence of BB transport in the FT impacting the vertical structure of ozone during this case study.

### 1. Introduction

Atmospheric chemistry over the Southeastern United States (SEUS) has attracted significant interest from the scientific community resulting in recent field campaigns conducted over the region, such as the Southeast Nexus (SENEX) [Warneke *et al.*, 2016] and the Studies of Emissions and Atmospheric Composition, Clouds and Climate Coupling by Regional Surveys (SEAC<sup>4</sup>RS) [Toon *et al.*, 2016]. The SEUS is distinctive due to large emissions of natural sources in this region interacting with anthropogenic emissions resulting in high air pollutant concentrations with a large effect of radiative forcing [Hidy *et al.*, 2014; Leibensperger *et al.*, 2012a, 2012b]. However, some detailed chemical mechanisms (e.g., isoprene-ozone chemistry) [Mao *et al.*, 2013] of the interaction between natural and anthropogenic emissions are not well understood causing significant uncertainty in predicting future air quality and climate change in response to human activities.

Biomass burning (BB) is an important process that affects tropospheric ozone [Galanter *et al.*, 2000; Lelieveld and Dentener, 2000] due to high emissions of ozone precursor species, primarily carbon monoxide (CO), volatile organic compounds (VOCs), and nitrogen oxides (NO<sub>x</sub>), and can negatively impact air quality [Jaffe *et al.*, 2004] and human health [Bell *et al.*, 2004]. Ozone production from BB is highly variable and dependent upon fire emissions, photochemistry, aerosol effects on chemistry and radiation, and meteorological patterns [Jaffe and Wigder, 2012; Parrington *et al.*, 2013]. Recent studies show that the BB smoke is frequently observed in the SEUS from both local fire sources [Liu *et al.*, 2016] and long-range transport from the western U.S. [Kim *et al.*, 2015]. Its impact on climate and surface air quality could be more significant than the previously determined [Zhang and Wang, 2016].

Stratosphere-to-troposphere transport (STT) or stratospheric intrusion is another important source for tropospheric ozone. STT results from various mechanisms such as tropopause folding [Shapiro, 1980], Rossby wave breaking [Merrill *et al.*, 1996; Thompson *et al.*, 2010], gravity wave breaking [Lamarque *et al.*, 1996], and convective “wrapping and shedding” [Pan *et al.*, 2014]. Based on model studies, STT is expected to experience a minimum in the summer for the extratropics in terms of both intrusion frequency [Elbern *et al.*, 1997] and net downward flux transport [Wernli and Bourqui, 2002] when summertime tropospheric ozone is largely controlled by in situ photochemistry [Lelieveld and Dentener, 2000]. The frequency of tropopause folding, which is the major process controlling STT, exhibits strong seasonal and geographic variations [Rao *et al.*, 2008; Sprenger *et al.*, 2003]. The detection of STT is sensitive to the selection of stratospheric tracers such as ozone [Bethan *et al.*, 1996], water vapor [Beekmann *et al.*, 1997], potential vorticity [James *et al.*, 2003], static stability [Pan *et al.*, 2009], and <sup>7</sup>Be [Elbern *et al.*, 1997]. Quantifying the cross-tropopause flux of stratospheric air to assess the impact of STT on the troposphere is highly sensitive to the parameterization of the intrusion process [Gettelman and Sobel, 2000; Hsu *et al.*, 2005]. Chemical transport models also display large uncertainties in STT processes, likely due to numerous factors resulting in the inability to consistently replicate observed ozone laminae [Roelofs *et al.*, 2003; Tarasick *et al.*, 2007]. The numerous observational and simulated uncertainties in summertime STT motivate the investigation of various tracers and meteorological parameters from detailed ground-based and airborne observations during a STT event during the summer in the SEUS.

STT and BB smoke transport seem to be two independent processes, and the simultaneous impact of these two processes on atmospheric chemical composition has been demonstrated in only few studies [e.g., Brioude *et al.*, 2007; Trickl *et al.*, 2015]. However, Langford *et al.* [2015] first argued that the dry air which descends from the upper troposphere and lower stratosphere (UTLS) during STT events is favorable for wild fires, and therefore, they could be indirectly related. Overall, both STT and BB influence at the surface are of scientific interest due to their capability to lead to significant increases in background ozone mixing ratios potentially resulting in air-quality exceedance events [Langford *et al.*, 2009; McKendry *et al.*, 2011; Morris *et al.*, 2006; Pfister *et al.*, 2008].

This work presents an analysis of coordinated airborne and ground-based measurements acquired in Alabama (AL) on 28 and 29 June 2013 during the SENEX investigation. The SENEX field campaign was designed to characterize emission sources, transport processes, and atmospheric chemistry impacting trace gases (e.g., ozone) and aerosol spatiotemporal variability in the summer months in the SEUS. During the SENEX campaign, on 28–29 June 2013 multiple instruments, both ground based and airborne, observed large ozone lamina over northern AL. The main objective of this study is to investigate detailed observations, from multiple instruments including ground-based ozone lidar and aerosol lidar, to identify and quantify the chemical signatures for trace gases and aerosols associated with STT and BB smoke transport processes.

## 2. Instruments

### 2.1. Ozone Lidar

The Rocket-city Ozone (O<sub>3</sub>) Quality Evaluation in the Troposphere (RO<sub>3</sub>QET) lidar is a differential absorption lidar (DIAL) located on the campus of the University of Alabama in Huntsville (UAH) at 34.725°N and 86.645°W at 206 m above sea level (asl). The RO<sub>3</sub>QET lidar is one of the six systems of the Tropospheric Ozone Lidar Network (TOLNet) (<http://www-air.larc.nasa.gov/missions/TOLNet>) and is also affiliated with the international Network for the Detection of Atmospheric Composition Change (<http://ndacc-lidar.org>). During the working period discussed in this paper, this system measured ozone from 0.1 km up to about

**Table 1.** Parameters of Raman Shifting for the UAH Laser Transmitter

First Stokes $\lambda$	Active Gas	Buffer Gas	Conversion Efficiency	First Stokes Energy
289 nm	445 psi D <sub>2</sub>	350 psi Helium	29%	7 mJ/pulse
299 nm	240 psi H <sub>2</sub>	240 psi Argon	40%	5 mJ/pulse

12 km during nighttime and up to approximately 5 km during daytime with a temporal resolution of 2 min. The vertical resolutions of the DIAL retrievals vary from 150 m in the lower troposphere to 750 m in the upper troposphere to maintain an acceptable signal-to-noise ratio (SNR) of lidar signal with altitude. Ozone lidars are uniquely capable of providing continuous, high-temporal-resolution measurements of ozone structures.

The DIAL technique derives ozone concentrations by analyzing how rapidly the backscattered signals at two separate but closely spaced wavelengths, one strongly absorbed by ozone and the other less strongly absorbed, diminish with altitude. This measurement does not require the absolute signal intensities but only the relative change of the two signals with respect to altitude. Minor hardware changes have been incorporated into this instrument compared to the earlier papers by *Kuang et al.* [2011, 2013]. The laser transmitter previously consisted of two Nd:YAG-pumped dye lasers to generate 285 and 291 nm ultraviolet (UV) lasers. The transmitter now comprises two Raman-shifted lasers at 289 and 299 nm (as of May 2013) for easier operation and higher measurable altitude. Two 30 Hz, 266 nm Nd:YAG lasers pump two 1.8 m Raman cells, respectively, with mixtures of active gas and buffer gas to generate 289 and 299 nm lasers. The parameters of the on-line (289 nm) and off-line (299 nm) wavelengths for the Raman shifting are listed in Table 1. Experiments with cell gas pressure and mixing ratio based on the previously reported experiments [*De Schouepnikoff et al.*, 1997; *Milton et al.*, 1998] dictate optimized conversion efficiency and beam quality. Hydrogen (H<sub>2</sub>) gas has a higher first Stokes conversion efficiency than deuterium (D<sub>2</sub>) for Raman shifting. Less energy is needed in the off-line channel due to less ozone absorption and Rayleigh scattering. Therefore, the pump laser energy for the off-line channel (H<sub>2</sub> cell) is reduced to half of its maximum to avoid near-range signal saturation issues.

An iterative aerosol correction [*Kuang et al.*, 2011] is applied to reduce errors arising from differential aerosol backscattering typically encountered below 6 km. The 289–299 nm wavelength pair has similar ozone differential absorption cross section as the 285–291 nm pair, however, is approximately 1.7 times more sensitive to aerosol interference compared to the 285–291 nm pair due to its larger wavelength separation [*Browell et al.*, 1985]. The receiving system consists of three receivers and four photomultiplier tubes similar to that described by *Kuang et al.* [2013] except that the solar filters have been replaced by the 300 nm short-pass filters for all telescopes accommodating the laser wavelength change. The integrated solar radiation below 300 nm is much higher than that below 292 nm so that the daytime highest measurable altitude is only about 5 km. The further modification of the high-altitude channel by adding narrowband solar filters [*McDermid et al.*, 2002] to extend the daytime measurable altitude was not completed before the time period of this study. By comprehensively considering these changes (e.g., larger SNR resulted by the longer wavelengths and higher filter transmission, potentially larger aerosol interference), we estimate the lidar measurement precision to be similar to that reported by *Kuang et al.* [2011],  $\pm 10\%$  in the lower troposphere and  $\pm 20\%$  in the upper troposphere.

## 2.2. Ozonesondes

The Huntsville electrochemical concentration cell-type [*Komhyr*, 1969] ozonesondes (ENSCI 2Z) used during this study measure ozone, temperature, pressure, and water vapor up to 35 km with a vertical resolution of 100 m [*Newchurch et al.*, 2003], a precision better than  $\pm 5\%$ , and an accuracy better than  $\pm 10\%$  [*Johnson et al.*, 2002; *Smit et al.*, 2007]. In addition to ozone, the ozonesonde measurement provides relative humidity (RH) data that can be used as a tropospheric-air tracer. The pressure and temperature measured by the collocated ozonesonde (usually an attached independent radiosonde) represent a more accurate atmospheric profile compared to a standard atmosphere assumption or sounding profile at other locations and, therefore, result in more accurate ozone lidar retrievals. The ozonesondes employ iMet radiosonde reporting Global Position System (GPS) altitude which is more accurate than pressure-temperature-RH-derived altitude [*Stauffer et al.*, 2014]. Previous intercomparison experiments suggest that iMet reports temperatures about 0.5°C lower and RH 1–2% wetter compared to the widely used Vaisala RS92 below 20 km [*Hurst et al.*, 2011]. These biases have negligible impact on this study.

**Table 2.** Measurements From the NOAA WP-3D Aircraft

Species	Technique	Sampling Interval	Accuracy	Lower Detection Limit	Reference
BC	Single-particle soot photometer	1 s	30%	0.5 fg	Schwarz <i>et al.</i> [2008 and 2010]
CO	Vacuum UV fluorescence	1 s	5%	0.5 ppbv	Holloway <i>et al.</i> [2000]
CH <sub>3</sub> CN	Proton Transfer Reaction Mass Spectrometer (PTR-MS)	1 s <sup>a</sup>	20%	35 pptv	de Gouw and Warneke [2007] and Warneke <i>et al.</i> [2015]
RH <sup>b</sup>	Chilled mirror hygrometer	1 s	5%	NA <sup>c</sup>	Warneke <i>et al.</i> [2016]
Ozone	Nitrogen-oxide (NO)-induced chemiluminescence detection	1 s	2%	15 pptv	Ryerson <i>et al.</i> [1998]

<sup>a</sup>Measured for 1 s interval every 14–18 s.

<sup>b</sup>Derived from dew point temperature.

<sup>c</sup>NA, not applicable.

### 2.3. HSRL

The University of Wisconsin's high spectral resolution lidar (HSRL) uses molecular scattering as a calibration reference to provide aerosol backscatter cross section, optical depth, and depolarization with a 7.5 m vertical resolution from the surface up to 15 km [Grund and Eloranta, 1991; Eloranta *et al.*, 2004]. This system deployed in Huntsville, AL, from 19 June to 4 November 2013 and operated almost 24 h every day to support both SENEX and SEAC<sup>4</sup>RS campaigns. Because of its high spatiotemporal resolution and continuous measurement capability, a lidar is an ideal instrument to capture the rapid variations of aerosols. Simultaneous ozone and aerosol vertical profile measurements provide unique information on their interactions and sources of pollutant transport [Browell *et al.*, 2003].

### 2.4. Airborne Sensors

The National Oceanic and Atmospheric Administration's (NOAA's) WP-3D aircraft has a range of 3000 km, a maximum altitude of 7.6 km and a speed of 115 m · s<sup>-1</sup>. During the SENEX field campaign, the aircraft had a typical flight duration of 7 h and an actual maximum altitude of 6.4 km due to heavy instrument payloads [Warneke *et al.*, 2016]. This study employs measurements of black carbon (BC), acetonitrile (CH<sub>3</sub>CN), carbon monoxide (CO), RH, and ozone made by the instruments onboard the WP-3D (see Table 2) for information of individual measurements. The accuracy for these measurements is typically estimated through intercomparison with data from other reliable or well-characterized instruments. Ozone was measured by a chemiluminescence instrument based on the reaction between ambient ozone and NO as a reagent gas. The fast-response CO measurement was made by a vacuum UV fluorescence instrument. The CH<sub>3</sub>CN and other volatile organic compounds (VOC) were measured by a proton transfer reaction mass spectrometer (PTR-MS) with a high sensitivity and fast time response. The aerosol measurements such as BC were conducted in a low-turbulence sampling inlet to minimize the impact from turbulence and improve the particle transmission [Wilson *et al.*, 2004]. The position and motion of the aircraft as well as many meteorological parameters such as RH were recorded with instruments installed by the NOAA Aircraft Operations Center flight facility.

## 3. Results

### 3.1. Meteorological Context

Meteorological conditions illustrated in the upper air analysis charts (Figure 1a) for 1200 UTC 28 June 2013 show an upper air extratropical cutoff cyclone centered over the border between the U.S. and Canada with one cold front and one stationary front at the surface (Figure 1b). In this paper, we will discuss only the cold front to the west of the large low-pressure center, extending from Ohio to northern Texas (see Figure 1b), which was approaching Huntsville, AL. The convective clouds on the leading edge of the cold front moving southeasterly had already reached Huntsville at 1200 UTC on 28 June. There was a moderate upper air jet stream between the high- and low-pressure centers on the 500 hPa level (see Figure 1a).

Figures 2a and 2b shows the backscatter and linear depolarization measured by HSRL on 28 and 29 June 2013. The cirrus clouds, which typically have high depolarization at about 40% [Eloranta, 2005], were observed by HSRL near 14 km at near 0830 UTC on 28 June. The cirrus cloud top is typically slightly below



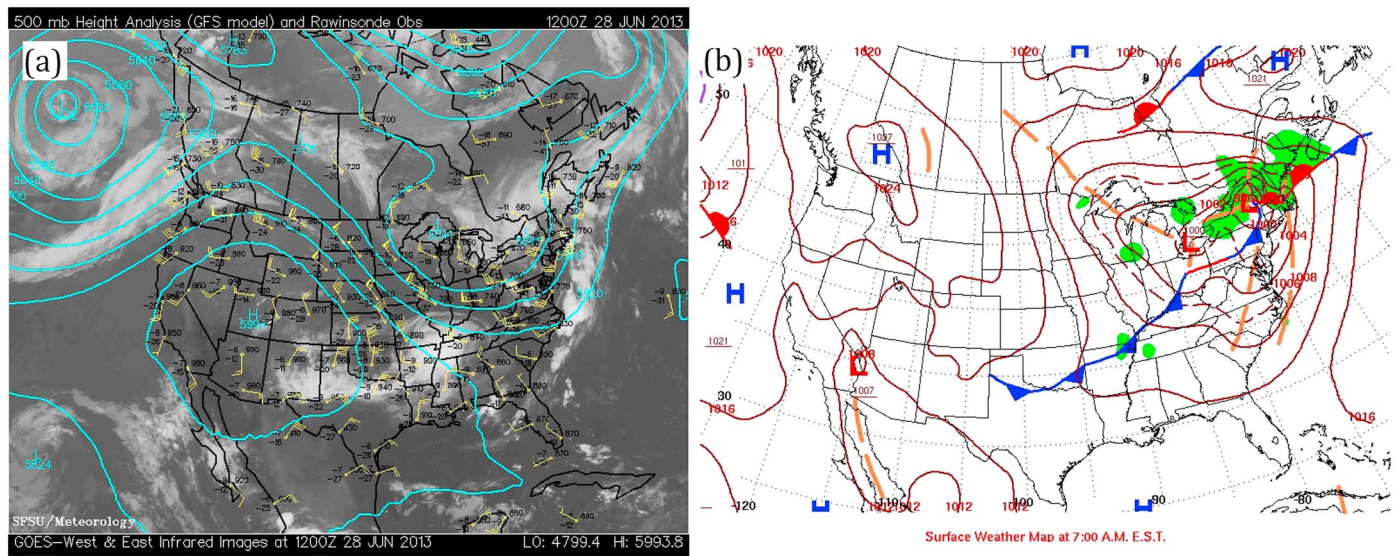


**Figure 1.** (a) Geostationary Operational Environmental [Menzel and Purdom, 1994] satellite-infrared image with Global Forecast System (<http://www.emc.ncep.noaa.gov/GFS>) analysis field provided by the National Center for Environmental Prediction (NCEP) of NOAA including wind vectors and geopotential heights at 500 hPa (<http://squall.sfsu.edu/>) and (b) NOAA/NCEP surface analysis map (<http://www.wpc.ncep.noaa.gov/dailywxmap/>), for 1200 UTC 28 June 2013 showing an upper air extratropical cutoff cyclone centered above the northeastern U.S. and its corresponding surface cold front approaching Huntsville.

the tropopause [Sassen *et al.*, 2008]. According to its depth and anvil structure measured by HSRL, the cirrus was likely produced by convective updrafts [Sassen and Campbell, 2001]. With the approach of the surface cold front and resultant convection, the cloud-base height descended to 5 km at 1730 UTC.

### 3.2. DIAL and HSRL Measurement Analysis

The HSRL curtains in Figures 2a and 2b revealed large aerosol concentrations in the planetary boundary layer (PBL) with an elevated aerosol layer at about 5 km from 0800 to 1600 UTC 28 June. At 1800 UTC, the strong convection removed the aerosols below 5 km when the center of the convective clouds approached Huntsville, and the cloud base appeared to be at its lowest. The DIAL measured ozone mixing ratios between 80 and 100 ppb below the cloud base as shown in Figure 2c, representing higher than summer average ozone for this altitude level (about 80 ppbv). Large ozone gradients at the upper air cold front suggest that not only meteorological variables but also trace gases exhibit discontinuity on the frontal zone [Pickering *et al.*, 1988]. The ozone beneath the cold front surface was about 40 ppb because the postfrontal air was transported from the northwest where lower tropospheric ozone is generally lower [Cooper *et al.*, 2001] and may not be affected by the STT. Typically, after a cold front passage, ozone decreases in the PBL due to precipitation, lower temperature, and higher wind speeds. Ozone significantly decreases in the lower free troposphere (FT) due to westerly advection and increases in the upper troposphere due to influence from the UTLS. The FT, including the lower FT, may have laminar enhancement structures arising from STT, which will be discussed later in this study.

The aerosol layers occurring in the FT up to 5 km before 0000 UTC 29 June had higher backscatter and were coupled with minimal ozone enhancement, compared to the lower tropospheric average, suggesting a fresh smoke or urban source. In Figure 2c, two free tropospheric (FT) ozone layers (with the one at about 3.5 km denoted as L2-1 and the one at about 5.5 km denoted as L2-2) with significant ozone enhancement compared to their surrounding areas, 30 ppb on average, were detected by the ozone lidar after 0000 on 29 June. The shape of L2-2 was highly correlated with the aerosol structures measured by the HSRL, while L2-1 was moderately correlated with the aerosols. Both L2-1 and L2-2 were likely influenced by aged smoke from BB due to their relatively low backscatter and low depolarization. The linear depolarization of aged smoke can be lower than fresh smoke [Burton *et al.*, 2012; Groß *et al.*, 2013] because the scavenging and deposition processes remove some of the large and nonspherical particles during transport. However, ozone enhancements due to BB alone will rarely reach 30 ppbv [e.g., Real *et al.*, 2007; Parrington *et al.*, 2013] even when ozone

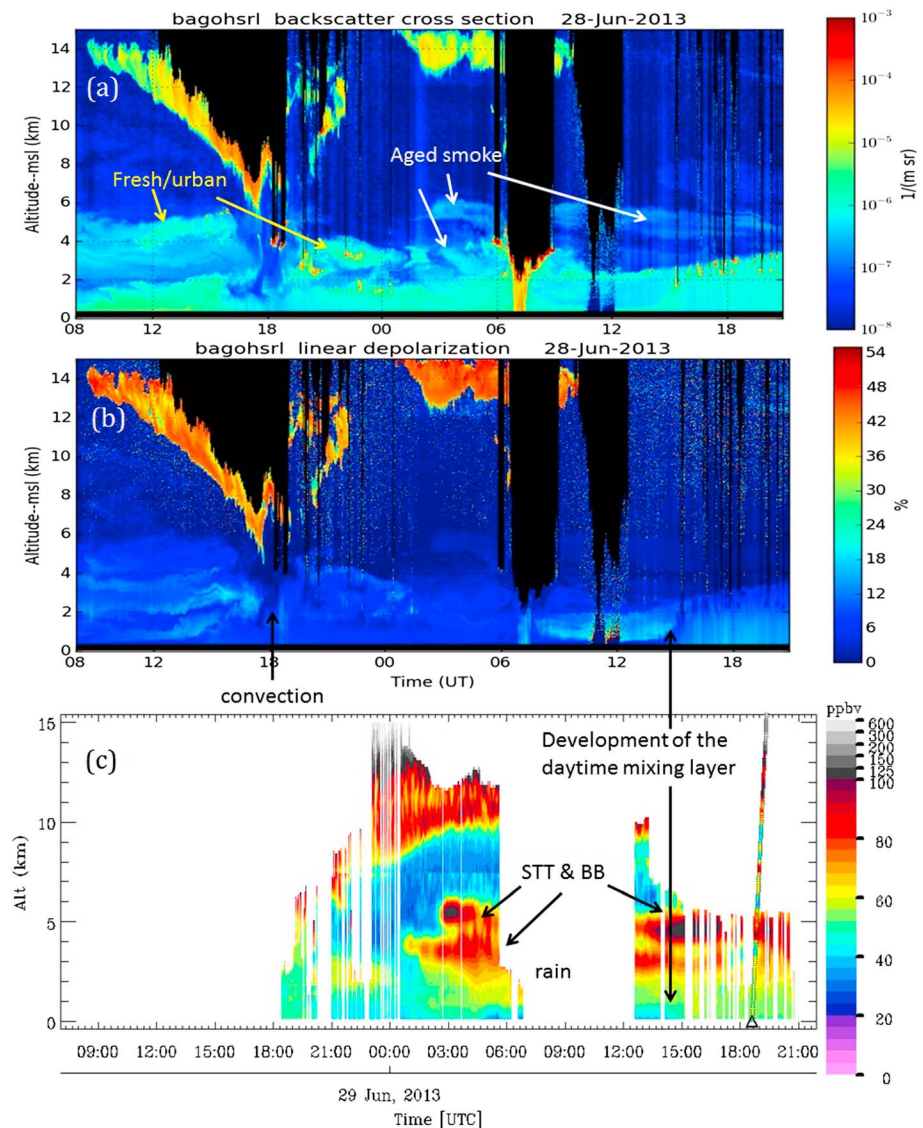


**Figure 2.** Coincident ozone lidar and HSRL observations on 28 and 29 June 2013, which suggest that the free tropospheric ozone at Huntsville was affected by both STT and smoke transport. (a) HSRL backscatter cross section, (b) HSRL linear depolarization, and (c) ozone mixing ratios. The black triangle represents the collocated ozonesonde profile.

production is very efficient at a low  $\text{NO}_x$  concentration [Hudman *et al.*, 2004]. Therefore, there may be other sources (which will be discussed later) responsible for the large ozone enhancement.

Multiple active fires occurred several days before 29 June. For example, the aerosol optical depth (AOD) [Remer *et al.*, 2005] and fire locations detected by the Moderate Resolution Imaging Spectroradiometer (MODIS) in Figures 3a and 3b show smoke in Nevada, Colorado, New Mexico, Nebraska, Texas, Arkansas, and Canada associated with fires on 27 or 28 June. We employ Hybrid Single-Particle Lagrangian Integrated Trajectory (HYSPLIT) [Rolph, 2016] backward trajectory ensemble calculation to explore possible sources for the smoke layers observed by the HSRL. This ensemble mode generates multiple trajectories at the same location. Each trajectory is computed by offsetting its initial meteorological grid by  $\pm 0.15$  factor (i.e.,  $0.15 \times 1$  km here) to account for calculation uncertainties arising from meteorological field input [Stein *et al.*, 2015]. Substantial HYSPLIT simulation experiments indicate that the trajectory ensemble for 4 km at ending at 1500 UTC 28 June in Figure 3c, mostly reflected by both horizontal advection and convectively uplifting movement, generally represents the trajectories for the smoke between 2 and 5 km observed by the HSRL before 0000 29 June. The accurate identification of the smoke source is difficult because these trajectories pass



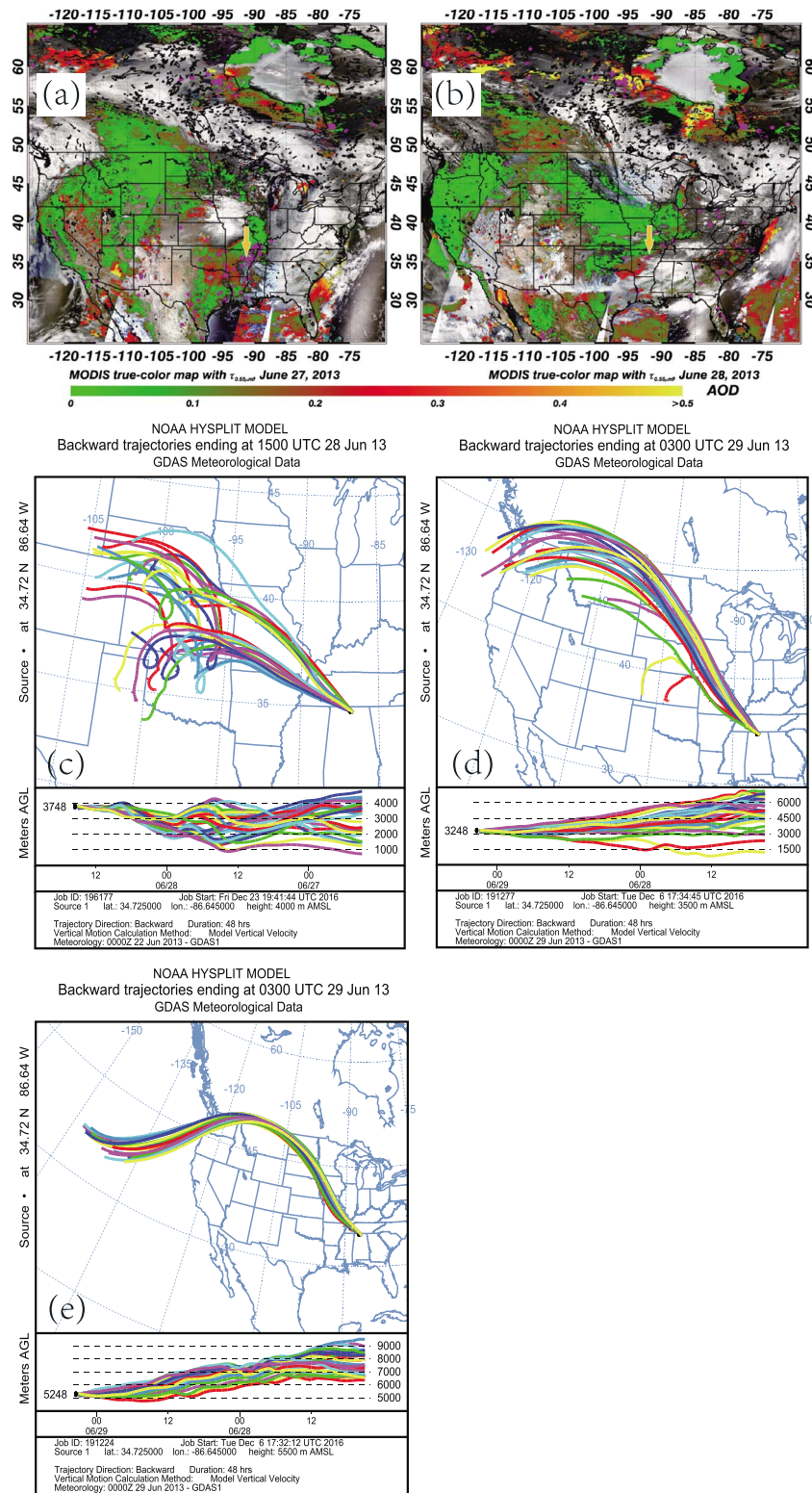


**Figure 3.** MODIS AOD at 550 nm overlaid MODIS Level 1B radiances from Terra Satellite on (a) 27 and (b) 28 June 2013. Clouds are shown in white, and AOD at 550 nm is shown in various colors ranging from green to yellow indicating low to high aerosol concentrations. The purple dots represent Terra-detected fire locations using the algorithm described by Giglio *et al.* [2003]. The arrows mark the likely source for the fresh smoke observed above Huntsville on June 29. 48 h HYSPLIT backward trajectory ensemble in Huntsville for the observed smoke layers at (c) 4 km asl at 15:00 UTC 28 June, (d) 3.5 km asl at 03:00 UTC 29 June, and (e) 5.5 km asl at 03:00 UTC 29 June.

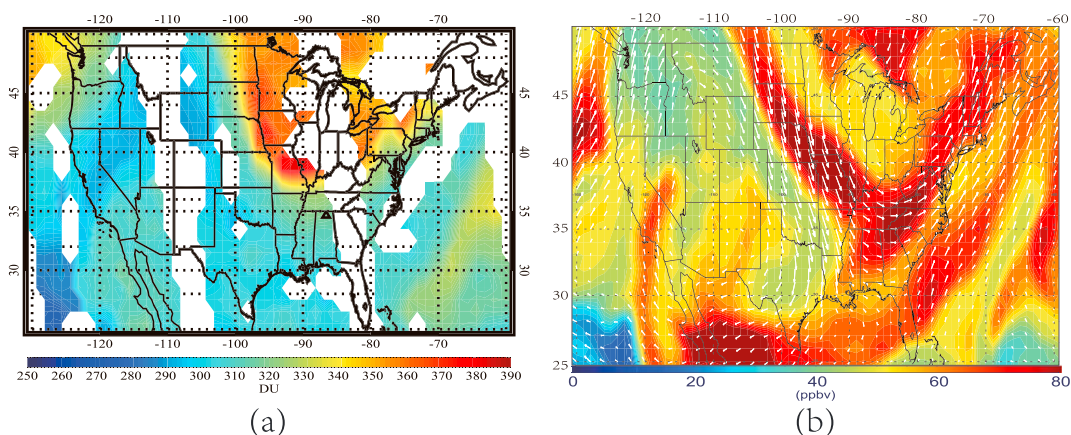


**Figure 4.** Satellite data and model calculations showing the influence of STT over Huntsville. (a) OMI total ozone column [Liu *et al.*, 2010] on 29 June 2013 gridded to a resolution of  $1^\circ$  longitude  $\times$   $1.25^\circ$  latitude. The blank area is missing data resulting from the OMI row anomaly. The black triangle represents Huntsville, AL. (b) Analysis field of the ozone mixing ratio at 5 km above ground level with resolution of  $1^\circ \times 1^\circ$  simulated by RAQMS for 1200 UTC 29 June 2013.

multiple active fire locations. However, we believe the most likely source for the fresh smoke was the agricultural burning near Arkansas because of three reasons. First, Figure 3c suggests major convection occurring between 1200 27 June and 1200 28 June when the air parcel passed Arkansas. The convection was helpful to lift the smoke from PBL to free troposphere. Second, smoke sourcing from Arkansas is supported by the animation of model-simulated CO from another chemistry model (not shown). Third, the fires in Arkansas were more significant and lasted longer than other possible fire sources as suggested by Figures 3a and 3b.

Figures 3d and 3e present the backward trajectories for the smoke layers observed at 3.5 km (L2-1 in Figure 2) and 5.5 km (L2-2 in Figure 2) at 0300 UTC 29 June. The sources for L2-1 and L2-2 are highly uncertain because these trajectories crossed many possible fire locations and these trajectories do not indicate major convection which is necessary to uplift the smoke from the PBL to free troposphere, especially for the 5.5 km back trajectories. However, these trajectories did not pass several major active fires in the southwestern U.S. such as the fires in Nevada, New Mexico, and Colorado (with even longer duration of HYSPLIT back trajectory), leaving the possibility that L2-1 and L2-2 originated from forest fires in western Canada. They were relatively aged and were probably transported from the PBL to the free troposphere some time earlier by convection which is not well captured by HYSPLIT. The HYSPLIT back trajectory analysis suggests that the observed smoke layers in the free troposphere before and after 0000 29 June sourced from different locations consistent with the earlier analysis of the HSRL measurements. The subsidence suggested by most trajectories in Figures 3d and 3e is distinctive to the mostly convective and horizontal motion in Figure 3c. This descending feature is rather robust after many sensitivity experiments of HYSPLIT modelling indicative of a highly likely influence from UTLS for L2-1 and L2-2. After the precipitation, ozone in L2-1 weakened around 0730 UTC on 29 June. Ozone generally has a negative correlation with RH because of heterogeneous loss of the catalysts in the ozone production chain, which are primarily hydrogen oxides ( $\text{HO}_x$ ) and nitrogen oxides ( $\text{NO}_x$ ) [Jacob, 2000]. However, L2-2 slowly descended without much reduction of its ozone concentration because it was located slightly above the nimbostratus. The low-ozone layer (about 45 ppbv), formed by  $\text{NO}_x$  titration in the nocturnal boundary layer, was quickly enhanced to about 55 ppbv with the development of the daytime convective mixing layer in the early morning (near 1430 UTC) due to downward mixing of higher-ozone amounts from higher altitudes. The horizontal structure of total ozone [Liu *et al.*, 2010] measured by the satellite-borne Ozone Monitoring Instrument (OMI) [Levelt *et al.*, 2006] in Figure 4a suggests the potential influence from stratospheric ozone at Huntsville on 29 June, although the impact of stratospheric ozone is not expected to be as large as spring or fall. Figure 4b presents the ozone analysis field with  $1^\circ \times 1^\circ$  resolution at 1200 UTC simulated by the Real-time Air Quality Modeling System (RAQMS) [Pierce *et al.*, 2007] showing that significant ozone enhancement at 5 km occurs at the places with the greatest total ozone gradients meaning these ozone enhancement were caused by STT [Wimmers *et al.*, 2003]. The background ozone at 5 km to the west of the low-pressure system simulated by RAQMS was approximately 40 ppbv consistent what the ozone lidar measured underneath the upper air frontal zone. The RAQMS model, with real-time

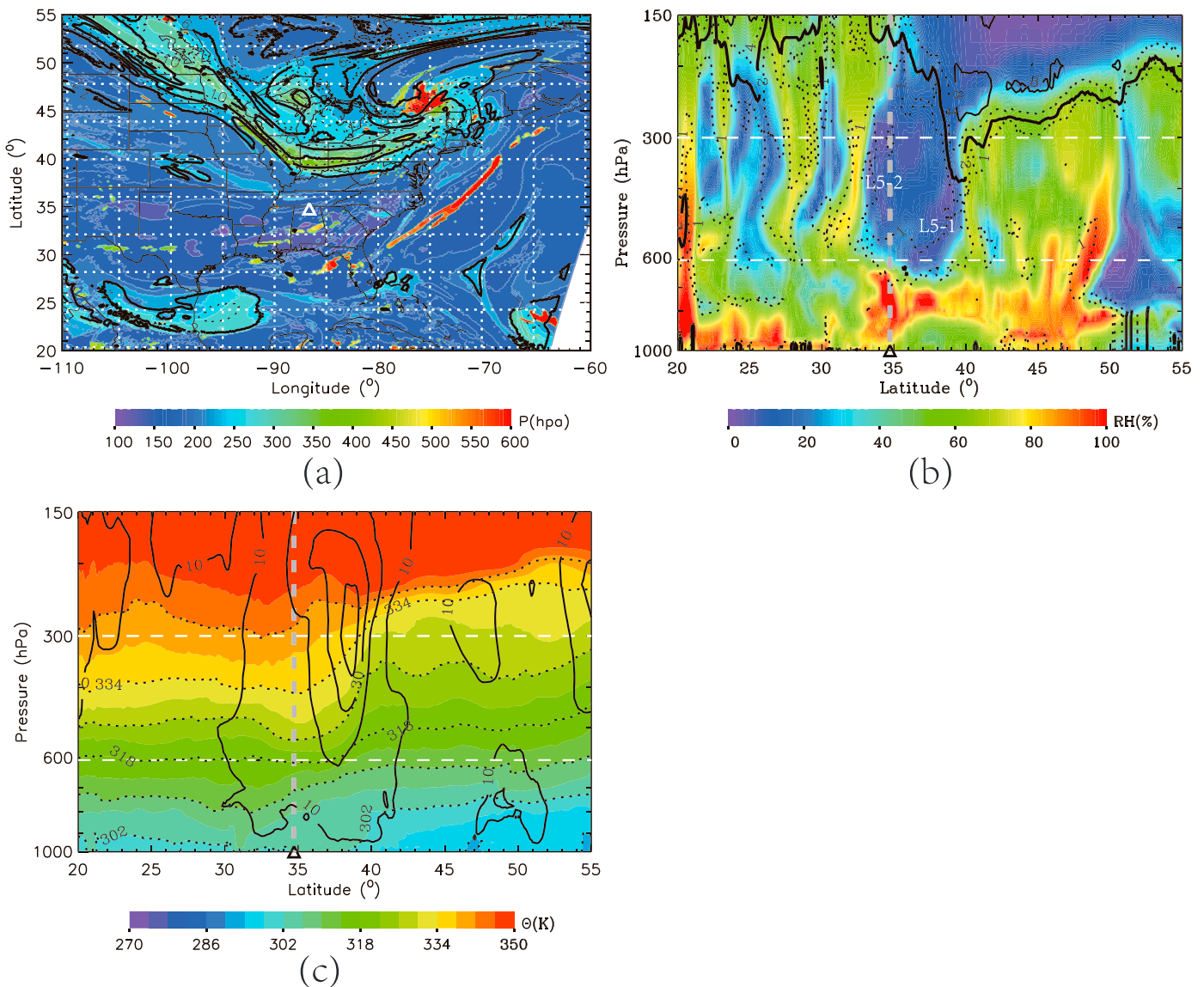


**Figure 5.** Meteorological structures derived from the NAM model showing the STT process caused by tropopause folding. (a) 340 K IPV (black dotted and solid interweaved lines) with a 2 PVU interval and the 2 PVU tropopause pressure (color contours) for 0000 29 June 2013. (b) Pressure-latitude cross section of IPV (black dotted and solid interweaved lines) and RH (color contours). L5-1 and L5-2 represent two dry layers associated with the STT process. (c) Pressure-latitude cross section of potential temperature (dotted lines) and wind speed (solid lines) at 86.645°W. The heavy solid line represents the 2 PVU tropopause or dynamic tropopause. The triangles represent the location of Huntsville.

satellite observations assimilated, has been shown to have the capability to capture both the dynamic and chemical features associated with STT events and provides good context for interpretation of the ozone observations [Langford et al., 2015; Yates et al., 2013].

### 3.3. Modeled Potential Vorticity Analysis

For further analysis of the dynamic characteristics of this STT process, we examine the meteorological fields from the North American Mesoscale (NAM) model from the National Centers for Environmental Prediction (NCEP) [Janjic, 2003]. The NAM outputs have a horizontal resolution of 13 km and 39 vertical pressure layers from 1000 to 50 hPa. Figure 5a presents the 340K isentropic potential vorticity (IPV) and the dynamic tropopause pressure at 0000 UTC on 29 June 2013. PV is widely used as a stratospheric tracer with the advantage of quantifying the air flux across the tropopause. The lowest 2 potential vorticity unit (PVU =  $10^{-6} \text{ K} \cdot \text{m}^2 \cdot \text{kg}^{-1} \cdot \text{s}^{-1}$ ) surface is considered as the dynamic tropopause [e.g., Lamarque and Hess,



1994]. The shape of the PV anomaly is closely associated with the cutoff cyclone with the maximum PV mostly located at the west flank as expected [Sprengrer *et al.*, 2007]. The dynamic tropopause relevant to our study stayed mostly higher than 400 hPa (about 7.5 km asl), and its lowest portion was located at north of 37°N. This is expected because the summertime STT processes generally occur farther to the north and higher in altitude compared to other seasons [Wernli and Bourqui, 2002]. In Figure 5b, the vertical cross section of PV and RH at the Huntsville longitude (86.645°W) clearly shows a tropopause fold occurring between 300 and 400 hPa at 40°N, slightly north of Huntsville. Two dry layers, L5-1 and L5-2, appear to the south of the fold. L5-1 was the dry air lamina directly associated with the fold at 40°N according to the PV and RH structures. L5-2, however, likely formed from another folding process which occurred earlier, based on analysis of the NAM calculations. The RH cross section in Figure 5b is consistent with the ozone lidar structure measured at Huntsville in Figure 2c. The dry tongue, L5-2, agrees with the enhanced ozone layer observed in the upper troposphere between 0000 and 0006 29 June 2013. Upper tropospheric air often contains a stratospheric component after the cold frontal passage due to tropopause folding [Cooper *et al.*, 2002; Fischer *et al.*, 2002]. Another dry layer, L5-1, extended as low as 600 hPa (about 4.3 km asl) and did not reach Huntsville at this time, 0000 UTC on 29 June, generally consistent with the observation for the enhanced ozone layers L2-1 and L2-2. Figure 5c shows the cross section of potential temperature and isotach. The upper air jet core was located south of the tropopause fold with maximum winds of 40 m/s. It is difficult to accurately know when and where the cross-tropopause transport happens. However, by assuming that the intense mixing between troposphere and stratosphere generally happens slightly above the dynamic tropopause in the extratropics [Pan *et al.*, 2004], the potential temperature for maximum STT occurred approximately at 330 K for this case, which was significantly higher than what was observed for springtime by Kuang *et al.* [2012]. This agrees with our expectation since the potential temperature for active STT in summer is higher than during other seasons [Sprengrer and Wernli, 2003] as a consequence of the seasonal variation of the location of the isentropic surface.

### 3.4. Ozonesonde Measurement Analysis

Figure 6a shows the ozonesonde measurement of temperature, RH, ozone, and its comparison to the DIAL. Because the ozonesonde ascended with a speed of approximately 5 m/s, the DIAL ozone measurements, 2 min integration time for raw data, were chosen with its closest time to the sonde at each altitude grid for a comparison purpose. The differences between the DIAL and ozonesonde measurements are less than 7% below 2 km, less than 13% within the PBL (<3.1 km), and maximize at 30% at 3.8 km by assuming the ozonesonde measurement is the true value. Their differences between 2 and 3 km are slightly larger than expected. We checked the DIAL profiles nearly coincident with the sonde measurement times and found that the DIAL measured ozone consistently about 10% higher than the ozonesonde between 2 and 3 km. This difference occurs because the DIAL data containing cloud interference have been discarded by the retrieval program; therefore, the DIAL-measured ozone was the values free of cloud. But the ozonesonde measured ozone inside the cloud between 2 and 3 km suggested by the high RH values in Figure 6a. Clouds usually reduce ozone because of wet removal of the catalysts in the ozone production chain [Jacob, 2000; Pickering *et al.*, 1991].

The discrepancies between DIAL and ozonesonde above 3 km may be attributed to both the instrument measurement uncertainties and drifting of the ozonesonde. The latter can be a dominant cause when large horizontal ozone gradients exist. The measurement discrepancies of the two instruments generally increasing with altitude are consistent with our expectation due to the statistical uncertainty of the lidar and ozonesonde measurements [Kuang *et al.*, 2011], balloon drifting distance from the lidar laboratory, and sonde measurement of the GPS geopotential height [Hurst *et al.*, 2011] all increase with altitude.

The ozonesonde profile in Figure 6a suggests a 3.1 km daytime PBL height, where a temperature inversion and large water vapor gradient exist, consistent with the PBL height estimated from the HSRL curtain plot in Figure 2a. Such a PBL height is significantly higher than the average expected from climatology, about 2 km for summertime SEUS [Seidel *et al.*, 2012]. Below the top of the PBL, ozone slightly increased with altitude. The laminar structure of the sonde-measured ozone above 3.4 km is result of insufficient mixing of horizontally advected air mass containing different ozone concentrations. A low ozone layer (minimum 40 ppbv) between 3.4 and 4.1 km was associated with moderate water vapor. Above another temperature inversion at 4.1 km, an enhanced ozone layer (80–90 ppbv) was associated with low RH, as low as 2%, typically suggesting a

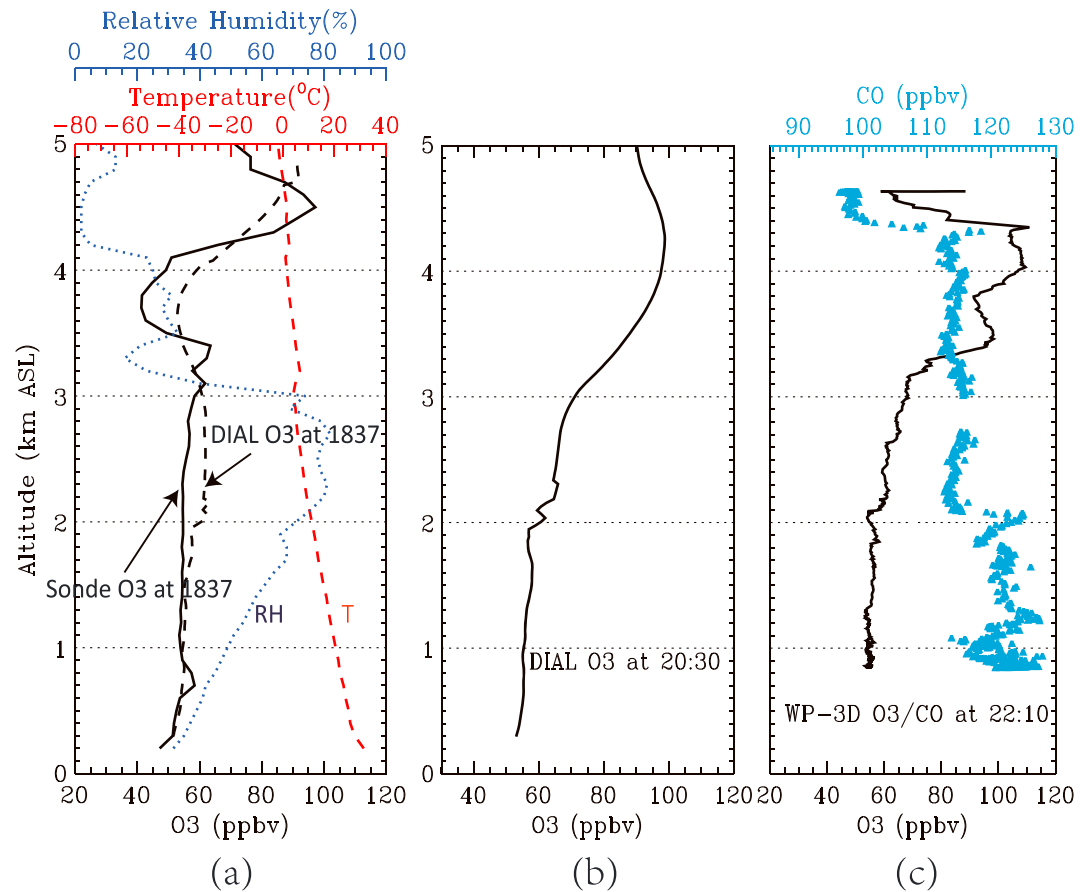


**Figure 6.** Ozonesonde, DIAL, and WP-3D measurements made in Huntsville on 29 June 2013 showing rapid ozone change above 3.4 km and unchanged ozone in the PBL. (a) Ozone, temperature, and RH measured by the ozonesonde launched at 1837 UTC and the simultaneous DIAL ozone profile. (b) The DIAL ozone profile at 2030 with a 10 min average. (c) The ozone and CO profiles measured by WP-3D at 2210.

stratospheric source with age from a few hours up to a few days [Sullivan et al., 2015; Trickl et al., 2014]. The dry air stream descended from near tropopause level and is often found in the upper air behind the front [Browning, 1997]. The influence from the stratosphere is consistent with our earlier analysis, but the affected altitudes might be slightly different due to differing measurement time and horizontal drifting of the ozonesonde. The ozone evolution in Figure 6 suggests the free tropospheric ozone changed significantly (up to 130% around 4 km) only in a few hours, mostly due to dynamics, while the PBL ozone did not change significantly.

### 3.5. WP-3D Airborne Measurement Analysis

The NOAA WP-3D airborne observations over Birmingham on 29 June shown in Figure 7 are consistent with the above analysis and confirm that the FT ozone in the 3 to 4.6 km range was affected by both STT and smoke. The airborne spiral measurements above Huntsville, with a spiral diameter of about 6 km, were taken between 2207 and 2219 UTC, about 1 h later than the lidar operation termination time and three and half hours later than the ozonesonde launch time. The spiral was performed 2.8 km to the north of the lidar lab and ozonesonde station as shown in Figure 7b. The WP-3D ozone and CO profiles shown in Figure 6 include only the spiral measurements. We will show measurements for more species over a larger area above Huntsville in a later section. On the WP-3D ozone profile in Figure 6c, large vertical gradients occurred just above 3 km consistent with the PBL height determined from the ozonesonde observations. The CO profile did not show a reduction immediately above the PBL top (between 3.1 and 4.3 km) as expected [Wagner et al., 2015], and ozone was enhanced by about 30 ppbv compared to the PBL suggesting enhancement from pollution in the FT. In contrast, the large CO reduction between 4.3 and 4.6 km was an indicator of unpolluted



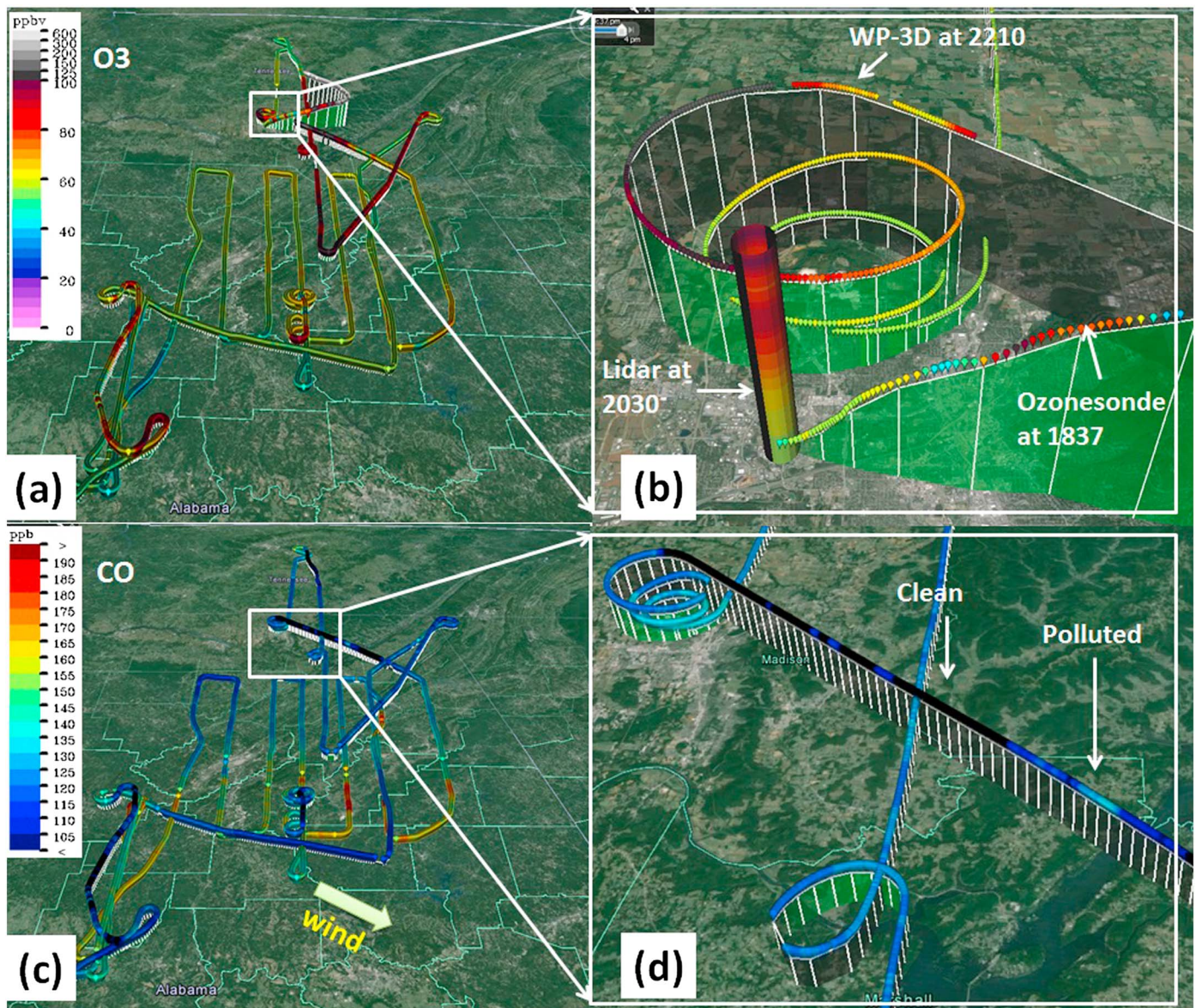


**Figure 7.** NOAA WP-3D airborne ozone and CO measurements during the Birmingham flight on 29 June 2013. (a) Overview of the ozone mixing ratios measured throughout the entire flight; (b) ozone profiles measured by WP-3D, lidar, and ozonesonde measurements in Huntsville; (c) overview of the CO mixing ratios measured by WP-3D; (d) CO mixing ratios measured by WP-3D east of Huntsville showing mixing of clean and polluted air at 4.6 km.

air which exhibited an unclear correlation between ozone and CO, especially varied ozone (also see large horizontal ozone gradients in Figure 7b) corresponding to unchanged CO at 4.6 km, reflecting a mixing of air from difference sources.

Figure 8 presents the P-3 measurements of chemical species over the Huntsville vicinity on 29 June to investigate the relationship between different species. The time frame of the spiral flight is marked by the vertical, solid gray lines. The variations of black carbon (BC) concentration across the PBL top, at about 3.1 km, clearly mark the distinction between mixed layer and FT. In the FT, we can see both signatures for BB and STT at 4.6 km slightly east of Huntsville although not directly above Huntsville. Between 2200 and 2203 UTC, the enhanced BC, CO, ozone, and CH<sub>3</sub>CN were positively correlated suggesting the BB influence. CO has been widely used as a tracer for BB because of its significant contribution to CO [Andreae and Merlet, 2001; Galanter et al., 2000]. CO can also be used to distinguish between tropospheric and stratospheric air by evaluating the ozone-CO relationship [Pan et al., 2004]. Different slopes of ozone to CO ratios are usually related

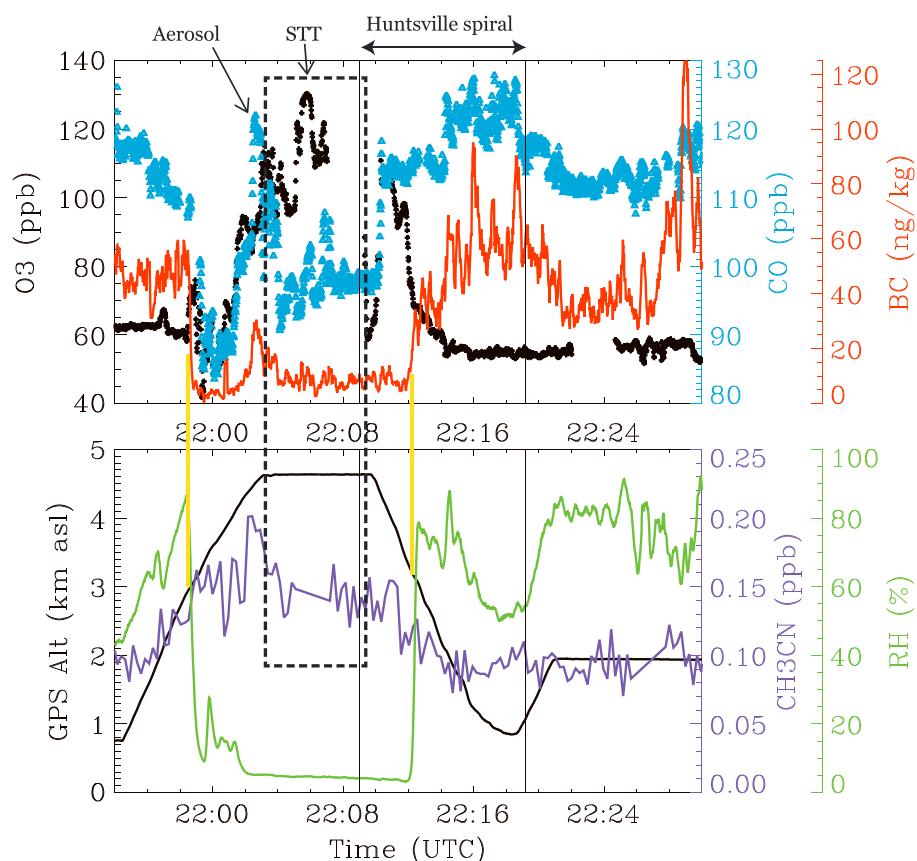


**Figure 8.** WP-3D measurements of chemical species over the Huntsville vicinity on 29 June 2013. A boxcar average with a 10 s window has been applied on the BC data. The solid gray lines represent the spiral measurements within Huntsville (used by Figure 6). The solid yellow lines represent the separation of measurements between the FT and the PBL. The air mass with anticorrelation between CO and ozone, measured between 2203 and 2209 and located east of Huntsville, is considered to be the stratospheric source (red in Figure 9b).

to different ages of the BB plumes [Macdonald *et al.*, 2011].  $\text{CH}_3\text{CN}$  is a good tracer for biomass burning [de Gouw *et al.*, 2003] due to its long lifetime, about 5 months [Hamm and Warneck, 1990], and lack of production in the urban plume [Holzinger *et al.*, 1999]. The air with  $\text{CH}_3\text{CN} > 150$  pptv can be defined as BB plume [Finch *et al.*, 2014]. For this flight, neither the peak  $\text{CH}_3\text{CN}$  (200 pptv) or peak CO (128 ppbv) was very high, probably because of dilution during transport for aged BB smoke. The RH in this lamina was mostly higher than 10% and higher than what was expected for stratospheric-source air.

On the other hand, the high ozone (132 ppbv) at 2206 corresponded to the low CO (approximately 80 ppbv) and low RH (5%) suggesting a stratospheric source [Hoor *et al.*, 2002; Pan *et al.*, 2006]. Although the CO in the pure stratospheric air is typically below 40 ppbv [Pan *et al.*, 2004], CO in the layer with a stratospheric source could contain more than 80 ppbv [Brioude *et al.*, 2006; Trickl *et al.*, 2014, 2016] due to its irreversible mixing with tropospheric air. The high ozone was not likely generated by lightning because of the low total reactive nitrogen ( $\text{NO}_x$ ) concentrations observed in this altitude range (not shown). The large ozone and CO horizontal gradients, at 4.6 km shown on Figure 8, can also be clearly seen slightly east of Huntsville in northern AL in Figure 7 indicating insufficient mixing of the polluted air from the troposphere and the clean air from the stratosphere. The significant ozone enhancement observed above 3.4 (Figure 6) can be explained by the northeasterly transport of the descending dry air from the near tropopause. Johnson *et al.* [2016] quantified the tropospheric ozone budget above Huntsville of the same case using a chemical transport model and found the ozone between 3 and 6 km for 29 June 2013 was on average ~60% from long-range transport and STT. Figure 9 presents the NOAA WP-3D airborne observations for the entire flight on 29 June 2013 used to investigate the average relationship between species. Ozone was weakly anticorrelated with CO in the PBL meaning that dynamic processes, such as advection and



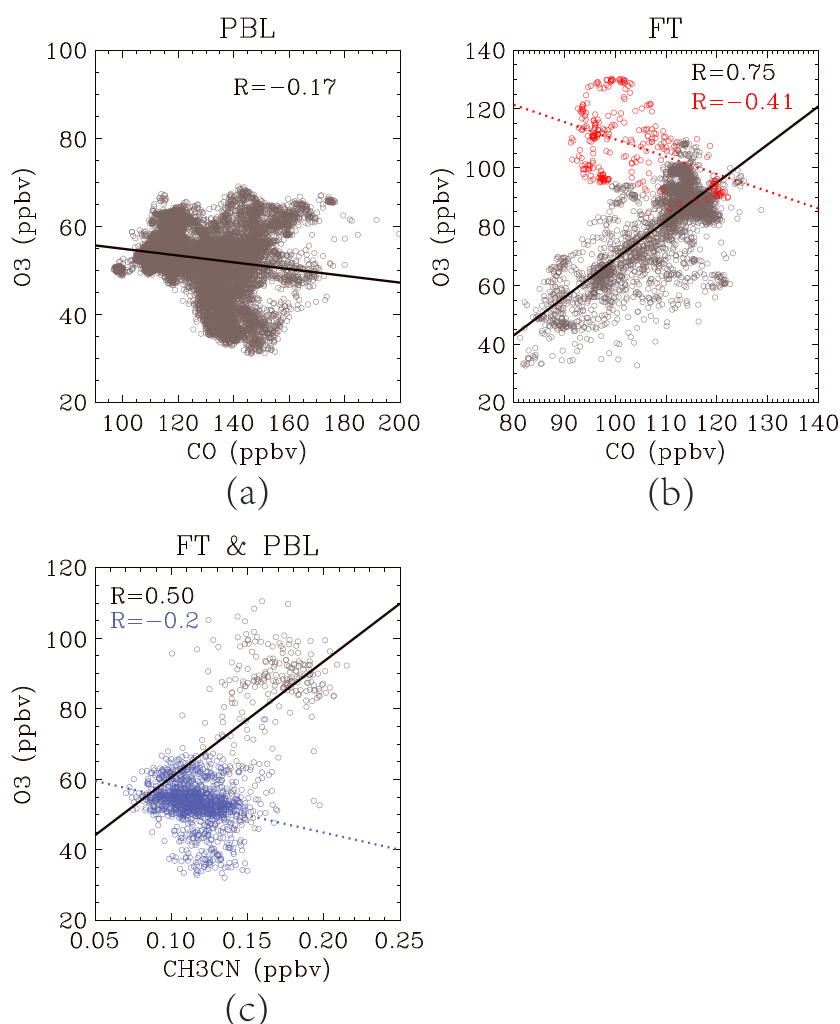


**Figure 9.** NOAA P-3 airborne chemistry observations for the entire flight on 29 June 2013. (a) O<sub>3</sub>-CO correlation in the PBL; (b) O<sub>3</sub>-CO correlation for BB source (gray,  $\Delta O_3/\Delta CO = 1.3 \text{ ppbv ppbv}^{-1}$ ) and stratospheric source (red); (c) O<sub>3</sub>-CH<sub>3</sub>CN correlation in the FT (gray,  $\Delta O_3/\Delta CH_3CN = 328 \text{ ppbv ppbv}^{-1}$ ) and PBL (purple). We consider altitudes  $>3100 \text{ m}$  in the FT and altitudes  $<3000 \text{ m}$  in the PBL.

convection, dominated in controlling the chemical distribution, and the photochemistry was relatively quiescent in the PBL. The quiescent photochemistry and lack of noticeable influence from the stratosphere for the PBL were also discovered for the entire month June in 2013 with low monthly PBL ozone average (53 ppbv) according to the Huntsville ozonesonde data. Ozone in the FT can be affected by both STT and transport of BB smoke. Therefore, we separate the air measured between 2203 and 2209 UTC and located at the east of Huntsville (marked by the dashed rectangle in Figure 8) as the STT-sourced air because of its moderately ( $R = -41\%$ ) anticorrelated ozone CO (as identified earlier). For other air masses in the FT, ozone was significantly correlated ( $R = 75\%$ ) with CO meaning a combustion source as precursors for ozone. The slope of the correlation,  $\Delta O_3/\Delta CO = 1.3 \text{ ppbv} \cdot \text{ppbv}^{-1}$ , is higher than other observations for summertime over North America [e.g., *Chin et al.*, 1994; *Mao et al.*, 2013; *Parrington et al.*, 2013] probably because of two reasons. First, this high production ratio can be found for the aged BB smoke [*Mauzerall et al.*, 1998; *Zhang et al.*, 2006]. Second, the approach where we manually separated the stratosphere is not accurate enough, so the “biomass-burning category” still included stratospheric-source ozone to result in a higher ratio. For the entire flight, the CH<sub>3</sub>CN average is much higher in the FT than the PBL reflecting a stronger influence in the FT from biomass burning transport. The moderate correlation between ozone and CH<sub>3</sub>CN ( $R = 50\%$ ) is also an evidence for the link between ozone and biomass burning in the FT, while the ozone was weakly anticorrelated ( $R = -20\%$ ) with CH<sub>3</sub>CN in the PBL.



In summary, we conclude the STT influence on the FT ozone at SEUS for 29 June 2013 according to the Huntsville ozonesonde profile and a small portion of the WP-3D airborne data made east of Huntsville with confirmation by the HYSPLIT back trajectory analysis, RAQMS ozone simulation, and NAM PV structures. The majority of the WP-3D data, however, shows a wide BB influence for the FT ozone at SEUS consistent with the ground-based HSRL aerosol and ozone DIAL observations at Huntsville. The identification of the ozone source attribution reflects a complex nature of atmospheric physics and chemistry.

#### 4. Discussion and Conclusions

The ground-based ozone lidar and HSRL measurements reveal detailed ozone structures at a SEUS site associated with a cold frontal passage. The tilted upper air frontal surface prohibited the direct exchange of the air mass at its two sides similar to *Pickering et al.*'s [1988] findings. The ozone below the front surface was significantly lower than that above. Two enhanced (+30 ppbv) ozone layers between 3 and 6 km behind the upper air cold front were captured by the ozone lidar. Further analysis from both the lidar and NOAA WP-3D measurements suggests that the ozone enhancement was caused by both STT and BB smoke transport. The dry ozone-rich air, originally from the stratosphere, mixed with the BB smoke behind the cold front [*Hudman et al.*, 2004; *Trickl et al.*, 2015] was the primary source of the enhanced ozone layers. The smoke could be produced by the wild fires in western Canada as suggested by the HYSPLIT back trajectory analysis with some uncertainties. The STT process was driven by a tropopause fold near 40°N associated with an upper air cutoff cyclone according to the PV analysis from the NAM model. Although the tropopause fold did not extend very deeply, its influence at low altitudes has been clearly observed indicative of the potential importance of summertime STT on the tropospheric ozone budget and on surface air quality [*Bachmeier et al.*, 1994; *He et al.*, 2011; *Merrill et al.*, 1996; *Sullivan et al.*, 2015; *Thompson et al.*, 2007].

The large horizontal ozone and CO gradients arising from insufficient mixing of the STT air and BB smoke were also captured by the NOAA WP-3D airborne observations about 45 km southeast of the Huntsville lidar laboratory. Statistical analysis of the WP-3D chemistry observations of the whole flight on 29 June indicates that ozone in the PBL was relatively low for summertime because of unfavorable meteorological conditions (e.g., high water vapor and strong convection) for ozone production and accumulation. The weak anticorrelation between CO and ozone in the PBL means quiescent photochemical production in the PBL consistent with the seasonal average characteristics in the lower troposphere at SEUS [*Wagner et al.*, 2015]. In the FT, however, ozone was significantly correlated with CO ( $R = 75\%$ ) and moderately correlated with the biomass burning tracer  $\text{CH}_3\text{CN}$  ( $R = 50\%$ ) indicative of influence of BB smoke transport. The relatively low CO, low  $\text{CH}_3\text{CN}$ , and high  $\Delta\text{O}_3/\Delta\text{CO}$  ratio ( $1.3 \text{ ppbv} \cdot \text{ppbv}^{-1}$ ) suggests that the BB smoke was highly aged. We note that the WP-3D touched only the lower edge of the 5 km aerosol layer observed by the HSRL, and the time of the WP-3D sampling in the FT was not long because the original target of this flight was PBL instead of FT. Therefore, the conclusion from the lower FT probably does not also apply to the middle and upper troposphere. The  $\text{RO}_3\text{QET}$  lidar agrees with the ozonesonde within 7% below 2 km and within 13% in the PBL ( $<3.1 \text{ km}$ ) as shown in Figure 6. After an analysis, we believe that this 13% difference is very likely real and caused by the fact that the ozonesonde measured ozone concentrations in a cloud layer lower than the ozone measured by  $\text{RO}_3\text{QET}$  lidar outside of clouds. The ozone difference between inside and outside of clouds may be worth further study [*Crawford et al.*, 2003], as noted in the discrepancy between the ozonesonde and DIAL measurements. The ozone evolution shown in Figures 2 and 6 exhibits stable ozone in the PBL and highly variable ozone in the FT for this case. The consistent ozone measurements within the PBL by all three instruments also suggest their accuracies in spite of no time overlap between the  $\text{RO}_3\text{QET}$  lidar and WP-3D measurements.

#### References

- Andrae, M. O., and P. Merlet (2001), Emission of trace gases and aerosols from biomass burning, *Global Biogeochem. Cycles*, 15(4), 955–966, doi:10.1029/2000GB001382.
- Bachmeier, A. S., M. C. Shipham, E. V. Browell, W. B. Grant, and J. M. Klassa (1994), Stratospheric/tropospheric exchange affecting the northern wetlands regions of Canada during summer 1990, *J. Geophys. Res.*, 99(D1), 1793–1804, doi:10.1029/93JD02179.
- Beekmann, M., et al. (1997), Regional and global tropopause fold occurrence and related ozone flux across the tropopause, *J. Atmos. Chem.*, 28, 29–44.
- Bell, M. L., A. McDermott, S. L. Zeger, J. M. Samet, and F. Dominici (2004), Ozone and short-term mortality in 95 US urban communities, 1987–2000, *J. Am. Med. Assoc.*, 292(19), 2372–2378.

#### Acknowledgments

The authors thank Whitney G. Jewett for editing the manuscript. The authors are grateful to Joshua P. Schwarz of NOAA/ESRL for providing the BC data. The authors thank the SENEX science team, instrument team, and pilot crew for managing and coordinating the intercomparison measurements. The authors also thank the MODIS team for providing the AOD, radiance, and fire data (AOD MOD04 10 km, Radiance MOD021KM 1 km, and Fires MOD14 1 km) and thank the NOAA Air Resources Laboratory (ARL) for the provision of the HYSPLIT model and READY website (<http://www.ready.noaa.gov>) used in this publication. The authors thank three anonymous reviewers for providing constructive comments. The ozone lidar data are available at <http://www-air.larc.nasa.gov/missions/TOLNet/>. This work is supported by the TOLNet program developed by National Aeronautics and Space Administration (NASA)'s Science Mission Directorate. The views, opinions, and findings contained in this report are those of the authors and should not be construed as an official NOAA, NASA, or the U.S. Government position, policy, or decision.

- Bethan, S., G. Vaughan, and S. J. Reid (1996), A comparison of ozone and thermal tropopause heights and the impact of tropopause definition on quantifying the ozone content of the troposphere, *Q. J. R. Meteorol. Soc.*, *122*, 929–944.
- Brioude, J., J. P. Cammas, and O. R. Cooper (2006), Stratosphere-troposphere exchange in a summertime extratropical low: Analysis, *Atmos. Chem. Phys.*, *6*(8), 2337–2353.
- Brioude, J., et al. (2007), Mixing between a stratospheric intrusion and a biomass burning plume, *Atmos. Chem. Phys.*, *7*(16), 4229–4235.
- Browell, E. V., S. Ismail, and S. T. Shipley (1985), Ultraviolet DIAL measurements of O<sub>3</sub> profiles in regions of spatially inhomogeneous aerosols, *Appl. Opt.*, *24*(17), 2827–2836.
- Browell, E. V., et al. (2003), Ozone, aerosol, potential vorticity, and trace gas trends observed at high-latitudes over North America from February to May 2000, *J. Geophys. Res.*, *108*(D4), 8369, doi:10.1029/2001JD001390.
- Browning, K. A. (1997), The dry intrusion perspective of extra-tropical cyclone development, *Meteorol. Appl.*, *4*(04), 317–324.
- Burton, S. P., R. A. Ferrare, C. A. Hostetler, J. W. Hair, R. R. Rogers, M. D. Obland, C. F. Butler, A. L. Cook, D. B. Harper, and K. D. Froyd (2012), Aerosol classification using airborne high spectral resolution lidar measurements—Methodology and examples, *Atmos. Meas. Tech.*, *5*, 73–98, doi:10.5194/amt-5-73-2012.
- Chin, M., D. J. Jacob, J. W. Munger, D. D. Parrish, and B. G. Doddridge (1994), Relationship of ozone and carbon monoxide over North America, *J. Geophys. Res.*, *99*(D7), 14,565–14,573, doi:10.1029/94JD00907.
- Cooper, O. R., J. L. Moody, D. D. Parrish, M. Trainer, T. B. Ryerson, J. S. Holloway, G. Hübler, F. C. Fehsenfeld, S. J. Oltmans, and M. J. Evans (2001), Trace gas signatures of the airstreams within North Atlantic cyclones: Case studies from the North Atlantic Regional Experiment (NARE '97) aircraft intensive, *J. Geophys. Res.*, *106*(D6), 5437–5456, doi:10.1029/2000JD900574.
- Cooper, O. R., J. L. Moody, D. D. Parrish, M. Trainer, T. B. Ryerson, J. S. Holloway, G. Hübler, F. C. Fehsenfeld, and M. J. Evans (2002), Trace gas composition of midlatitude cyclones over the western North Atlantic Ocean: A conceptual model, *J. Geophys. Res.*, *107*(D7), 4056–4068, doi:10.1029/2001JD000901.
- Crawford, J., et al. (2003), Clouds and trace gas distributions during TRACE-P, *J. Geophys. Res.*, *108*(D21), 8818, doi:10.1029/2002JD003177.
- de Gouw, J. A., C. Warneke, D. D. Parrish, J. S. Holloway, M. Trainer, and F. C. Fehsenfeld (2003), Emission sources and ocean uptake of acetonitrile (CH<sub>3</sub>CN) in the atmosphere, *J. Geophys. Res.*, *108*(D11), 4329, doi:10.1029/2002JD002897.
- de Gouw, J., and C. Warneke (2007), Measurements of volatile organic compounds in the earth's atmosphere using proton-transfer-reaction mass spectrometry, *Mass Spectrom. Rev.*, *26*(2), 223–257.
- De Schouepnikoff, L., V. Mitev, V. Simeonov, B. Calpini, and H. Van Den Bergh (1997), Experimental investigation of high-power single-pass Raman shifters in the ultraviolet with Nd: YAG and KrF lasers, *Appl. Opt.*, *36*(21), 5026–5043.
- Elbern, H., J. Kowol, R. Sladkovic, and A. Ebel (1997), Deep stratospheric intrusions: A statistical assessment with model guided analyses, *Atmos. Environ.*, *31*(19), 3207–3226.
- Eloranta, E. W. (2005), High spectral resolution lidar, in *Lidar: Range-Resolved Optical Remote Sensing of the Atmosphere*, edited by C. Weitkamp, pp. 143–163, Springer Science & Business, New York, NY.
- Eloranta, E. W., I. A. Razenkov, J. P. Garcia, and J. Hedrick (2004), Observations with the University of Wisconsin arctic high spectral resolution lidar, Proceedings of the 22nd International Laser Radar Conference, 561, 305–308, Matera, Italy.
- Finch, D. P., P. I. Palmer, and M. Parrington (2014), Origin, variability and age of biomass burning plumes intercepted during BORTAS-B, *Atmos. Chem. Phys.*, *14*(24), 13,789–13,800.
- Fischer, H., et al. (2002), Synoptic tracer gradients in the upper troposphere over central Canada during the Stratosphere-Troposphere Experiments by Aircraft Measurements 1998 summer campaign, *J. Geophys. Res.*, *107*(D8), 4064, doi:10.1029/2000JD000312.
- Galanter, M., H. Levy, and G. R. Carmichael (2000), Impacts of biomass burning on tropospheric CO, NO<sub>x</sub>, and O<sub>3</sub>, *J. Geophys. Res.*, *105*(D5), 6633–6653, doi:10.1029/1999JD901113.
- Gettelman, A., and A. H. Sobel (2000), Direct diagnoses of stratosphere-troposphere exchange, *J. Atmos. Sci.*, *57*, 3–16.
- Giglio, L., J. Descloitres, C. O. Justice, and Y. J. Kaufman (2003), An enhanced contextual fire detection algorithm for MODIS, *Remote Sens. Environ.*, *87*(2), 273–282.
- Groß, S., M. Esselborn, B. Weinzierl, M. Wirth, A. Fix, and A. Petzold (2013), Aerosol classification by airborne high spectral resolution lidar observations, *Atmos. Chem. Phys.*, *13*, 2487–2505, doi:10.5194/acp-13-2487-2013.
- Grund, C. J., and E. W. Eloranta (1991), University of Wisconsin high spectral resolution lidar, *Opt. Eng.*, *30*(1), 6–12.
- Hamm, S., and P. Warneck (1990), The interhemispheric distribution and the budget of acetonitrile in the troposphere, *J. Geophys. Res.*, *95*(D12), 20,593–20,606, doi:10.1029/JD095iD12p20593.
- He, H., et al. (2011), Transport analysis of ozone enhancement in Southern Ontario during BAQS-Met, *Atmos. Chem. Phys.*, *11*, 2569–2583, doi:10.5194/acp-11-2569-2011.
- Hidy, G. M., C. L. Blanchard, K. Baumann, E. Edgerton, S. Tanenbaum, S. Shaw, E. Knipping, I. Tombach, J. Jansen, and J. Walters (2014), Chemical climatology of the southeastern United States, 1999–2013, *Atmos. Chem. Phys.*, *14*(21), 11,893–11,914.
- Holloway, J. S., R. O. Jakoubek, D. D. Parrish, C. Gerbig, A. Volz-Thomas, S. Schmitgen, A. Fried, B. Wert, B. Henry, and J. R. Drummond (2000), Airborne intercomparison of vacuum ultraviolet fluorescence and tunable diode laser absorption measurements of tropospheric carbon monoxide, *J. Geophys. Res.*, *105*(D19), 24,251–24,261, doi:10.1029/2000JD900237.
- Holzinger, R., C. Warneke, A. Hansel, A. Jordan, W. Lindinger, D. H. Scharffe, G. Schade, and P. J. Crutzen (1999), Biomass burning as a source of formaldehyde, acetaldehyde, methanol, acetone, acetonitrile, and hydrogen cyanide, *Geophys. Res. Lett.*, *26*(8), 1161–1164, doi:10.1029/1999GL900156.
- Hoor, P., H. Fischer, L. Lange, J. Lelieveld, and D. Brunner (2002), Seasonal variations of a mixing layer in the lowermost stratosphere as identified by the CO–O<sub>3</sub> correlation from in situ measurements, *J. Geophys. Res.*, *107*(D5), 4044, doi:10.1029/2000JD000289.
- Hsu, J., M. J. Prather, and O. Wild (2005), Diagnosing the stratosphere-to-troposphere flux of ozone in a chemistry transport model, *J. Geophys. Res.*, *110*, D19305, doi:10.1029/2005JD006045.
- Hudman, R. C., et al. (2004), Ozone production in transpacific Asian pollution plumes and implications for ozone air quality in California, *J. Geophys. Res.*, *109*, D23S10, doi:10.1029/2004JD004974.
- Hurst, D. F., E. G. Hall, A. F. Jordan, L. M. Miloshevich, D. N. Whiteman, T. Leblanc, D. Walsh, H. Vömel, and S. J. Oltmans (2011), Comparisons of temperature, pressure and humidity measurements by balloon-borne radiosondes and frost point hygrometers during MOHAVE-2009, *Atmos. Meas. Tech.*, *4*, 2777–2793.
- Jacob, D. J. (2000), Heterogeneous chemistry and tropospheric ozone, *Atmos. Environ.*, *34*(12–14), 2131–2159.
- Jaffe, D. A., and N. L. Wigder (2012), Ozone production from wildfires: A critical review, *Atmos. Environ.*, *51*, 1–10.
- Jaffe, D., I. Bertsch, L. Jaeglé, P. Novelli, J. S. Reid, H. Tanimoto, R. Vingarzan, and D. L. Westphal (2004), Long-range transport of Siberian biomass burning emissions and impact on surface ozone in western North America, *Geophys. Res. Lett.*, *31*, L16106, doi:10.1029/2004GL020093.

- James, P., A. Stohl, C. Forster, S. Eckhardt, P. Seibert, and A. Frank (2003), A 15-year climatology of stratosphere–troposphere exchange with a Lagrangian particle dispersion model. 2. Mean climate and seasonal variability, *J. Geophys. Res.*, *108*(D22), 8522, doi:10.1029/2002JD002639.
- Janjic, Z. I. (2003), A nonhydrostatic model based on a new approach, *Meteorol. Atmos. Phys.*, *82*, 15, doi:10.1007/s00703-001-0587-6.
- Johnson, B. J., S. J. Oltmans, H. Vömel, H. G. J. Smit, T. Deshler, and C. Kroger (2002), Electrochemical concentration cell (ECC) ozonesonde pump efficiency measurements and tests on the sensitivity to ozone of buffered and unbuffered ECC sensor cathode solutions, *J. Geophys. Res.*, *107*(D19), 4393, doi:10.1029/2001JD000557.
- Johnson, M. S., S. Kuang, L. Wang, and M. J. Newchurch (2016), Evaluating summer-time ozone enhancement events in the southeast United States, *Atmosphere*, *7*(8), 108.
- Kim, P. S., et al. (2015), Sources, seasonality, and trends of southeast US aerosol: an integrated analysis of surface, aircraft, and satellite observations with the GEOS-Chem chemical transport model, *Atmos. Chem. Phys.*, *15*(18), 10,411–10,433.
- Komhyr, W. D. (1969), Electrochemical cells for gas analysis, *Ann. Geophys.*, *25*, 203–210.
- Kuang, S., J. F. Burris, M. J. Newchurch, S. Johnson, and S. Long (2011), Differential absorption lidar to measure subhourly variation of tropospheric ozone profiles, *IEEE Trans. Geosci. Remote Sens.*, *49*, 557–571, doi:10.1109/TGRS.2010.2054834.
- Kuang, S., M. J. Newchurch, J. Burris, L. Wang, K. Knupp, and G. Huang (2012), Stratosphere-to-troposphere transport revealed by ground-based lidar and ozonesonde at a midlatitude site, *J. Geophys. Res.*, *117*, D18305, doi:10.1029/2012JD017695.
- Kuang, S., M. J. Newchurch, J. Burris, and X. Liu (2013), Ground-based lidar for atmospheric boundary layer ozone measurements, *Appl. Opt.*, *52*, 3557–3566, doi:10.1364/AO.52.003557.
- Lamarque, J.-F., and P. G. Hess (1994), Cross-tropopause mass exchange and potential vorticity budget in a simulated tropopause folding, *J. Atmos. Sci.*, *51*, 2246–2269.
- Lamarque, J.-F., A. O. Langford, and M. H. Proffitt (1996), Cross-tropopause mixing of ozone through gravity wave breaking: Observation and modeling, *J. Geophys. Res.*, *101*(D17), 22,969–22,976, doi:10.1029/96JD02442.
- Langford, A. O., K. C. Aikin, C. S. Eubank, and E. J. Williams (2009), Stratospheric contribution to high surface ozone in Colorado during springtime, *Geophys. Res. Lett.*, *36*, L12801, doi:10.1029/2009GL038367.
- Langford, A. O., R. B. Pierce, and P. J. Schultz (2015), Stratospheric intrusions, the Santa Ana winds, and wildland fires in Southern California, *Geophys. Res. Lett.*, *42*, 6091–6097, doi:10.1002/2015GL064964.
- Leibensperger, E. M., L. J. Mickley, D. J. Jacob, W. T. Chen, J. H. Seinfeld, A. Nenes, P. J. Adams, D. G. Streets, N. Kumar, and D. Rind (2012a), Climatic effects of 1950–2050 changes in US anthropogenic aerosols—Part 1: Aerosol trends and radiative forcing, *Atmos. Chem. Phys.*, *12*(7), 3333–3348.
- Leibensperger, E. M., L. J. Mickley, D. J. Jacob, W. T. Chen, J. H. Seinfeld, A. Nenes, P. J. Adams, D. G. Streets, N. Kumar, and D. Rind (2012b), Climatic effects of 1950–2050 changes in US anthropogenic aerosols—Part 2: Climate response, *Atmos. Chem. Phys.*, *12*(7), 3349–3362.
- Lelieveld, J., and F. J. Dentener (2000), What controls tropospheric ozone? *J. Geophys. Res.*, *105*, 3531–3551, doi:10.1029/1999JD901011.
- Levelt, P. F., G. H. J. van den Oord, M. R. Dobber, A. Mäilki, H. Visser, J. de Vries, P. Stammes, J. O. V. Lundell, and H. Saari (2006), The Ozone Monitoring Instrument, *IEEE Trans. Geosci. Remote Sens.*, *44*, 1093–1101, doi:10.1109/TGRS.2006.872333.
- Liu, X., P. K. Bhartia, K. Chance, R. J. D. Spurr, and T. P. Kurosu (2010), Ozone profile retrievals from the Ozone Monitoring Instrument, *Atmos. Chem. Phys.*, *10*, 2521–2537, doi:10.5194/acp-10-2521-2010.
- Liu, X., et al. (2016), Agricultural fires in the southeastern U.S. during SEAC<sup>4</sup>RS: Emissions of trace gases and particles and evolution of ozone, reactive nitrogen, and organic aerosol, *J. Geophys. Res. Atmos.*, *121*, 7383–7414, doi:10.1002/2016JD025040.
- Macdonald, A. M., K. G. Anlauf, W. R. Leaitch, E. Chan, and D. W. Tarasick (2011), Interannual variability of ozone and carbon monoxide at the Whistler high elevation site: 2002–2006, *Atmos. Chem. Phys.*, *11*, 11,431–11,446, doi:10.5194/acp-11-11431-2011.
- Mao, J., F. Paulot, D. J. Jacob, R. C. Cohen, J. D. Crouse, P. O. Wennberg, C. A. Keller, R. C. Hudman, M. P. Barkley, and L. W. Horowitz (2013), Ozone and organic nitrates over the eastern United States: Sensitivity to isoprene chemistry, *J. Geophys. Res. Atmos.*, *118*, 11,256–11,268, doi:10.1002/jgrd.50817.
- Mauzerall, D. L., J. A. Logan, D. J. Jacob, B. E. Anderson, D. R. Blake, J. D. Bradshaw, B. Heikes, G. W. Sachse, H. Singh, and B. Talbot (1998), Photochemistry in biomass burning plumes and implications for tropospheric ozone over the tropical South Atlantic, *J. Geophys. Res.*, *103*(D7), 8401–8423, doi:10.1029/97JD02612.
- McDermid, I. S., G. Beyerle, D. A. Haner, and T. Leblanc (2002), Redesign and improved performance of the tropospheric ozone lidar at the Jet Propulsion Laboratory Table Mountain Facility, *Appl. Opt.*, *41*(36), 7550–7555.
- McKendry, I., et al. (2011), Californian forest fire plumes over Southwestern British Columbia: Lidar, sunphotometry, and mountaintop chemistry observations, *Atmos. Chem. Phys.*, *11*, 465–477, doi:10.5194/acp-11-465-2011.
- Menzel, W. P., and J. F. Purdom (1994), Introducing GOES-I: The first of a new generation of geostationary operational environmental satellites, *Bull. Am. Meteorol. Soc.*, *75*(5), 757–781.
- Merrill, J. T., J. L. Moody, S. J. Oltmans, and H. Levy II (1996), Meteorological analysis of tropospheric ozone profiles at Bermuda, *J. Geophys. Res.*, *101*(D22), 29,201–29,211, doi:10.1029/95JD03432.
- Milton, M. J. T., et al. (1998), Raman-shifted laser sources suitable for differential-absorption lidar measurements of ozone in the troposphere, *Appl. Phys. B*, *66*(1), 105–113.
- Morris, G. A., et al. (2006), Alaskan and Canadian forest fires exacerbate ozone pollution over Houston, Texas, on 19 and 20 July 2004, *J. Geophys. Res.*, *111*, D24503, doi:10.1029/2006JD007090.
- Newchurch, M. J., M. A. Ayoub, S. Oltmans, B. Johnson, and F. J. Schmidlin (2003), Vertical distribution of ozone at four sites in the United States, *J. Geophys. Res.*, *108*(D1), 4031, doi:10.1029/2002JD002059.
- Pan, L. L., W. J. Randel, B. L. Gary, M. J. Mahoney, and E. J. Hints (2004), Definitions and sharpness of the extratropical tropopause: A trace gas perspective, *J. Geophys. Res.*, *109*, D23103, doi:10.1029/2004JD004982.
- Pan, L. L., P. Konopka, and E. V. Browell (2006), Observations and model simulations of mixing near the extratropical tropopause, *J. Geophys. Res.*, *111*, D05106, doi:10.1029/2005JD006480.
- Pan, L. L., W. J. Randel, J. C. Gille, W. D. Hall, B. Nardi, S. Massie, V. Yudin, R. Khosravi, P. Konopka, and D. Tarasick (2009), Tropospheric intrusions associated with the secondary tropopause, *J. Geophys. Res.*, *114*, D10302, doi:10.1029/2008JD011374.
- Pan, L. L., et al. (2014), Thunderstorms enhance tropospheric ozone by wrapping and shedding stratospheric air, *Geophys. Res. Lett.*, *41*, 7785–7790, doi:10.1002/2014GL061921.
- Parrington, M., et al. (2013), Ozone photochemistry in boreal biomass burning plumes, *Atmos. Chem. Phys.*, *13*, 7321–7341, doi:10.5194/acp-13-7321-2013.
- Pfister, G. G., C. Wiedinmyer, and L. K. Emmons (2008), Impacts of the fall 2007 California wildfires on surface ozone: Integrating local observations with global model simulations, *Geophys. Res. Lett.*, *35*, L19814, doi:10.1029/2008GL034747.

- Pickering, K. E., R. R. Dickerson, G. J. Huffman, J. F. Boatman, and A. Schanot (1988), Trace gas transport in the vicinity of frontal convective clouds, *J. Geophys. Res.*, *93*(D1), 759–773, doi:10.1029/JD093iD01p00759.
- Pickering, K. E., A. M. Thompson, J. R. Scala, W.-K. Tao, J. Simpson, and M. Garstang (1991), Photochemical ozone production in tropical squall line convection during NASA Global Tropospheric Experiment/Amazon Boundary Layer Experiment 2A, *J. Geophys. Res.*, *96*(D2), 3099–3114, doi:10.1029/90JD02284.
- Pierce, R. B., et al. (2007), Chemical data assimilation estimates of continental US ozone and nitrogen budgets during INTEX-A, *J. Geophys. Res.*, *112*, D12S21, doi:10.1029/2006JD007722.
- Rao, T. N., J. Arvelius, and S. Kirkwood (2008), Climatology of tropopause folds over a European Arctic station (Esrangle), *J. Geophys. Res.*, *113*, D00B03, doi:10.1029/2007JD009638.
- Real, E., et al. (2007), Processes influencing ozone levels in Alaskan forest fire plumes during long-range transport over the North Atlantic, *J. Geophys. Res.*, *112*, D10S41, doi:10.1029/2006JD007576.
- Remer, L. A., et al. (2005), The MODIS aerosol algorithm, products, and validation, *J. Atmos. Sci.*, *62*(4), 947–973.
- Roelofs, G. J., et al. (2003), Intercomparison of tropospheric ozone models: Ozone transport in a complex tropopause folding event, *J. Geophys. Res.*, *108*(D12), 8529, doi:10.1029/2003JD003462.
- Rolph, G. D. (2016), *Real-Time Environmental Applications and Display System (READY)*, NOAA Air Resources Laboratory, College Park, Md. [Available at <http://www.ready.noaa.gov>.]
- Ryerson, T. B., et al. (1998), Emissions lifetimes and ozone formation in power plant plumes, *J. Geophys. Res.*, *103*(D17), 22,569–22,583, doi:10.1029/98JD01620.
- Sassen, K., and J. R. Campbell (2001), A midlatitude cirrus cloud climatology from the Facility for Atmospheric Remote Sensing. Part I: Macrophysical and synoptic properties, *J. Atmos. Sci.*, *58*(5), 481–496.
- Sassen, K., Z. Wang, and D. Liu (2008), Global distribution of cirrus clouds from CloudSat/Cloud-Aerosol Lidar and Infrared Pathfinder Satellite Observations (CALIPSO) measurements, *J. Geophys. Res.*, *113*, D00A12, doi:10.1029/2008JD009972.
- Schwarz, J. P., et al. (2008), Measurement of the mixing state, mass, and optical size of individual black carbon particles in urban and biomass burning emissions, *Geophys. Res. Lett.*, *35*, L13810, doi:10.1029/2008GL033968.
- Schwarz, J. P., et al. (2010), The detection efficiency of the single particle soot photometer, *Aerosol Sci. Technol.*, *44*, 612–628.
- Seidel, D. J., Y. Zhang, A. Beljaars, J.-C. Golaz, A. R. Jacobson, and B. Medeiros (2012), Climatology of the planetary boundary layer over the continental United States and Europe, *J. Geophys. Res.*, *117*, D17106, doi:10.1029/2012JD018143.
- Shapiro, M. A. (1980), Turbulent mixing within tropopause folds as a mechanism for the exchange of the chemical constituents between the stratosphere and troposphere, *J. Atmos. Sci.*, *37*, 10.
- Smit, H. G. J., et al. (2007), Assessment of the performance of ECC-ozonesondes under quasi-flight conditions in the environmental simulation chamber: Insights from the Juelich Ozone Sonde Intercomparison Experiment (JOSIE), *J. Geophys. Res.*, *112*, D19306, doi:10.1029/2006JD007308.
- Springer, M., and H. Wernli (2003), A northern hemispheric climatology of cross-tropopause exchange for the ERA15 time period (1979–1993), *J. Geophys. Res.*, *108*(D12), 8521, doi:10.1029/2002JD002636.
- Springer, M., M. Croci Maspoli, and H. Wernli (2003), Tropopause folds and cross-tropopause exchange: A global investigation based upon ECMWF analyses for the time period March 2000 to February 2001, *J. Geophys. Res.*, *108*(D12), 8518, doi:10.1029/2002JD002587.
- Springer, M., H. Wernli, and M. Bourqui (2007), Stratosphere-troposphere exchange and its relation to potential vorticity streamers and cutoffs near the extratropical tropopause, *J. Atmos. Sci.*, *64*(5), 1587–1602.
- Stauffer, R. M., G. A. Morris, A. M. Thompson, E. Joseph, G. J. Coetzee, and N. R. Nalli (2014), Propagation of radiosonde pressure sensor errors to ozonesonde measurements, *Atmos. Meas. Tech.*, *7*(1), 65–79.
- Stein, A. F., R. R. Draxler, G. D. Rolph, B. J. B. Stunder, M. D. Cohen, and F. Ngan (2015), NOAA's HYSPLIT atmospheric transport and dispersion modeling system, *Bull. Am. Meteorol. Soc.*, *96*(12), 2059–2077.
- Sullivan, J. T., T. J. McGee, A. M. Thompson, R. B. Pierce, G. K. Sumnitch, L. W. Twigg, E. Eloranta, and R. M. Hoff (2015), Characterizing the lifetime and occurrence of stratospheric-tropospheric exchange events in the rocky mountain region using high-resolution ozone measurements, *J. Geophys. Res. Atmos.*, *120*, 12,410–12,424, doi:10.1002/2015JD023877.
- Tarasick, D. W., et al. (2007), Comparison of Canadian air quality forecast models with tropospheric ozone profile measurements above midlatitude North America during the IONS/ICARTT campaign: Evidence for stratospheric input, *J. Geophys. Res.*, *112*, D12S22, doi:10.1029/2006JD007782.
- Thompson, A. M., et al. (2007), Intercontinental Chemical Transport Experiment Ozonesonde Network Study (IONS) 2004: 2. Tropospheric ozone budgets and variability over northeastern North America, *J. Geophys. Res.*, *112*, D12S13, doi:10.1029/2006JD007670.
- Thompson, A. M., et al. (2010), Convective and wave signatures in ozone profiles over the equatorial Americas: Views from TC4 2007 and SHADOZ, *J. Geophys. Res.*, *115*, D00J23, doi:10.1029/2009JD012909.
- Toon, O. B., et al. (2016), Planning, implementation, and scientific goals of the Studies of Emissions and Atmospheric Composition, Clouds and Climate Coupling by Regional Surveys (SEAC<sup>4</sup>RS) field mission, *J. Geophys. Res. Atmos.*, *121*, 4967–5009, doi:10.1002/2015JD024297.
- Trickl, T., H. Vogelmann, H. Giehl, H. E. Scheel, M. Sprenger, and A. Stohl (2014), How stratospheric are deep stratospheric intrusions? *Atmos. Chem. Phys.*, *14*(18), 9941–9961.
- Trickl, T., H. Vogelmann, H. Flentje, and L. Ries (2015), Stratospheric ozone in boreal fire plumes—The 2013 smoke season over central Europe, *Atmos. Chem. Phys.*, *15*, 9631–9649, doi:10.5194/acp-15-9631-2015.
- Trickl, T., et al. (2016), How stratospheric are deep stratospheric intrusions? LUAMI 2008, *Atmos. Chem. Phys.*, *16*, 8791–8815, doi:10.5194/acp-16-8791-2016.
- Wagner, N. L., et al. (2015), In situ vertical profiles of aerosol extinction, mass, and composition over the southeast United States during SENEX and SEAC<sup>4</sup>RS: Observations of a modest aerosol enhancement aloft, *Atmos. Chem. Phys.*, *15*, 7085–7102, doi:10.5194/acp-15-7085-2015.
- Warneke, C., et al. (2015), PTR-QMS versus PTR-TOF comparison in a region with oil and natural gas extraction industry in the Uintah Basin in 2013, *Atmos. Meas. Tech.*, *8*, 411–420.
- Warneke, C., et al. (2016), Instrumentation and measurement strategy for the NOAA SENEX aircraft campaign as part of the Southeast Atmosphere Study 2013, *Atmos. Meas. Tech.*, *9*(7), 3063–3093, doi:10.5194/amt-9-3063-2016.
- Wernli, H., and M. Bourqui (2002), A Lagrangian “1-year climatology” of (deep) cross-tropopause exchange in the extratropical Northern Hemisphere, *J. Geophys. Res.*, *107*(D2), 4021, doi:10.1029/2001JD000812.
- Wilson, J. C., B. G. Lafleu, H. Hilbert, W. R. Seebaugh, J. Fox, D. W. Gesler, C. A. Brock, B. J. Huebert, and J. Mullen (2004), Function and performance of a low turbulence inlet for sampling supermicron particles from aircraft platforms, *Aerosol Sci. Technol.*, *38*(8), 790–802.

- Wimmers, A. J., J. L. Moody, E. V. Browell, J. W. Hair, W. B. Grant, C. F. Butler, M. A. Fenn, C. C. Schmidt, J. Li, and B. A. Ridley (2003), Signatures of tropopause folding in satellite imagery, *J. Geophys. Res.*, *108*(D4), 8360, doi:10.1029/2001JD001358.
- Yates, E. L., L. T. Iraci, M. C. Roby, R. B. Pierce, M. S. Johnson, P. J. Reddy, J. M. Tadić, M. Loewenstein, and W. Gore (2013), Airborne observations and modeling of springtime stratosphere-to-troposphere transport over California, *Atmos. Chem. Phys.*, *13*(24), 12,481–12,494.
- Zhang, L., et al. (2006), Ozone-CO correlations determined by the TES satellite instrument in continental outflow regions, *Geophys. Res. Lett.*, *33*, L18804, doi:10.1029/2006GL026399.
- Zhang, Y., and Y. Wang (2016), Climate-driven ground-level ozone extreme in the fall over the southeast United States, *Proc. Natl. Acad. Sci. U.S.A.*, *113*(36), 10,025–10,030, doi:10.1073/pnas.1602563113.